Journal of Fluids and Structures 103 (2021) 103297

Contents lists available at ScienceDirect

Journal of Fluids and Structures

journal homepage: www.elsevier.com/locate/jfs

Vortex-induced vibration of elliptic cylinders and the suppression using mixed-convection

Hui Wan [a,*], Jeffrey A. DesRoches [b,c], Anthony N. Palazotto [c], Soumya S. Patnaik [b]

[a] Department of Mechanical and Aerospace Engineering, University of Colorado at Colorado Springs, 1420 Austin Bluffs Pkwy, Colorado Springs CO, 80918, USA
[b] Power and Control Division, Aerospace Systems Directorate, Air Force Research Laboratory, Wright-Patterson AFB, OH 45433, USA
[c] Department of Aeronautics and Astronautics, Graduate School of Engineering and Management, Air Force Institute of Technology, 2950 Hobson Way, Wright-Patterson AFB, OH 45433, USA

ARTICLE INFO

Article history:
Received 22 June 2020
Received in revised form 5 March 2021
Accepted 20 April 2021
Available online 29 April 2021

Keywords:
Mixed-convection
Vortex-induced vibration
Thermal control
Fluid–body interactions

ABSTRACT

Transverse vortex-induced vibration (VIV) of a two-dimensional, elliptic cylinder with various aspect ratios and stiffness is studied. The cylinder is elastically mounted and heated, and the flow direction is aligned with the direction of the thermal-induced buoyancy force. The transverse VIV can be suppressed as the thermal control parameter, the Richardson number (Ri), increases. Complete suppression is achieved when Ri is above a critical value, Ri_c. The critical Ri increases with the aspect ratio. For elliptic cylinders in lock-in regime, Ri_c is the optimal value since both VIV suppression and the minimum drag are achieved. A maximum drag reduction of 50.2% was found for an aspect ratio (AR) 2 cylinder at Ri_c. For VIV in the unsynchronized regime, even though the thermal control can suppress the vibration, the corresponding drag coefficient, however, can be higher than that in the case of without control. Therefore, the thermal control is more effective to suppress VIV in the lock-in regime. When suppressing the vibration of an AR 4 cylinder in the flexible VIV regime using thermal control, we observed the cross-2S vortex mode, in which the typical 2S vortices generated at near field can cross the centerline and switch sides after a few vibration cycles.

1. Introduction

The vortex-induced vibration (VIV) of a circular cylinder has broad applications in mechanical, aerospace, and civil engineering such as heat transfer, energy harvesting, and stability of structures. Properties of vortex shedding and VIV suppression have been thoroughly investigated (Sarpkaya, 2004; Williamson and Govardhan, 2004). The VIV characterization of an elliptic cylinder is relatively rare in literatures. Navrose et al. (2014) numerically studied the vortex-induced vibration of elliptical cylinders with aspect ratio ranging from 0.7 to 1.43. They found that the peak amplitude of cylinder oscillation increases with the aspect ratio (AR). Also, an elliptic cylinder whose major axis is aligned perpendicular to the free-stream flow experiences larger amplitude of oscillation compared to the case when the major axis is aligned parallel to the flow. With AR fixed at 1.5, Leontini et al. (2018) investigated VIV of a light elliptic body at various angles of attack. They found that when the angle of attack is smaller than 30°, the VIV response is similar to that of the circular cylinder. For large angle of attack, the flow has distinct asymmetric mode. Griffith et al. (2016) studied the passive

* Corresponding author.
E-mail addresses: hwan@uccs.edu (H. Wan), desroche@usna.edu (J.A. DesRoches), palazotto@sbcglobal.net (A.N. Palazotto), soumya.patnaik.1@us.af.mil (S.S. Patnaik).

https://doi.org/10.1016/j.jfluidstructs.2021.103297
0889-9746/

Nomenclature

AR	Aspect Ratio
A_x	Oscillation Amplitude
a, b	Major, and minor semi-axis of elliptic cylinder
C_x	y-direction force coefficient
C_y	y-direction force coefficient
$\overline{C}_y$	Time-averaged y-direction force coefficient
D	Characteristic length, $D = 2a$
D_h	Hydraulic diameter
f	Vibration frequency
f_n	Natural frequency of body
k	Spring constant of solid body
m	Mass of solid body
M_{red}	Reduced mass
Q_x	Nondimensional displacement
Re	Reynolds number
p	Nondimensional pressure
Pr	Prandtl number
Ri	Richardson number
Ri_c	Critical Richardson number
T_w	body temperature
T_∞	Incoming flow temperature
t	Nondimensional time
U	Free stream velocity
U_{red}	Reduced velocity
$\mathbf{u}$	Nondimensional velocity
θ	Nondimensional temperature
ρ_s, ρ_f	Density of solid and fluid
ν	Kinematic viscosity
κ	Thermal diffusivity
β	Thermal expansion coefficient

transverse motion of elastically mounted cylinders, which were actively controlled by prescribed rotational oscillation. It was found that both the amplitude and velocity of the transverse oscillation increase as the cylinder changes from circular to elliptical shape. Zhu et al. (2018) studied VIV of an elliptic cylinder that was free-to-rotate about its center and transverse in two other directions. The torsional friction was found to be a key factor in determining both the rotation response and the vibration amplitude. It is also found that the rotatable cylinder vibrates more vigorously compared to the non-rotatable elliptic cylinder. The free transverse and rotational vibration of elliptic cylinders was also investigated by Wang et al. (2019). They found that, under the rotation effect, the transverse peak amplitude at AR $= 1.0$ is 20% higher than its 1-DOF transverse-only counterpart. Zhao et al. (2019) studied dynamic response of elliptic cylinders undergoing transverse VIV. The aspect ratio ranged from 0.67 to 1.5. It was found that there existed two separated lock-in regimes for the lowest aspect ratio 0.67. They also reported that the vibration amplitude increased with the elliptical ratio, same observation as from Navrose et al. (2014). Hence, elliptic cylinders may experience larger VIV, compared to the circular cylinder. Suppressing VIV of elliptic cylinders needs to be investigated.

Generally, methods of VIV suppression are categorized as either passive or active. Passive suppression usually changes the body surface geometry by using stripes or tripping wires (Hover et al., 2001), small control bodies (Strykowski and Sreenivasan, 1990), splitter in the near wake of the main body (Dash et al., 2020; Kwon and Choi, 1996; Serson et al., 2014), or using wavy bodies (Assi and Bearman, 2018). Active suppression requires energy input to the system such as blowing/suction-based flow control (Chen et al., 2013; Wang et al., 2016b), synthetic jets (Wang et al., 2016a), piezoelectric devices (Adhikari et al., 2020; Franzini and Bunzel, 2018; Lee et al., 2019), and mixed convection (Garg et al., 2019a,b; Wan and Patnaik, 2016). For circular cylinders of various reduced mass, by aligning the flow direction with the direction of thermal-induced buoyance force, (Wan and Patnaik, 2016) found that there exists an optimal Richardson number that can fully suppress VIV, and simultaneously have the minimum drag generation. Garg et al. (2019a) investigated the case that the thermal buoyancy direction is particular to the flow direction. They found that the suppression of VIV can be achieved through thermal control only at small Reynolds number such as 50.

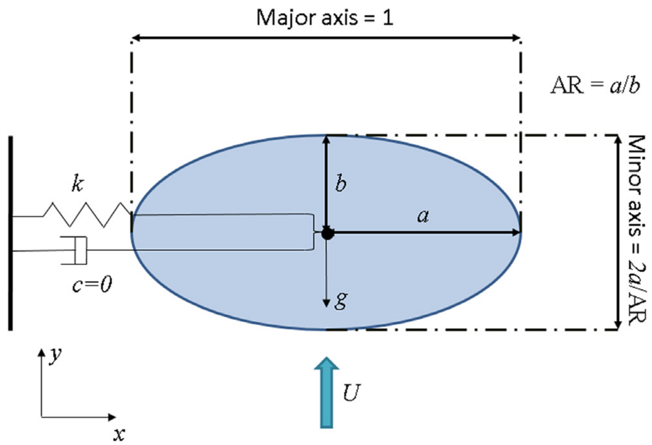

Fig. 1. Schematic of a 2D, elastically-mounted elliptic cylinder with 1-DOF. The body only vibrate in x-direction. The major axis is always set equal to unity. The depicted AR is 2, and g is gravity acceleration.

The objectives of the present study on VIV of elliptic cylinders are two aspects. First, extend the range of the aspect ratio of the elliptic cylinders. The aspect ratio ranges from 0.75 to 4 in this study. Second, evaluate the effectiveness of thermal control on suppressing the VIV of elliptic cylinders with various stiffness. Thus, the lock-in and unsynchronized regimes of elliptic cylinders with various ARs will be identified first. Then the thermal control is to be used to suppress VIV, and the corresponding flow field and drag generation will be investigated.

2. Mathematical formulation

The incompressible flow past over an elliptic cylinder can be described by the non-dimensional Navier–Stokes equation with Boussinesq approximation (Adhikari et al., 2020) and the energy equation, i.e.,

$$\nabla \cdot \mathbf{u} = 0 \tag{1}$$

$$\frac{\partial \mathbf{u}}{\partial t} + \mathbf{u} \cdot \nabla \mathbf{u} = -\nabla p + \frac{1}{Re}\nabla^2 \mathbf{u} + Ri\theta \tag{2}$$

$$\frac{\partial \theta}{\partial t} + \mathbf{u} \cdot \nabla \theta = \frac{1}{RePr}\nabla^2 \theta \tag{3}$$

in which $\mathbf{u}$, p, and θ are the non-dimensional velocity, pressure, and temperature, respectively. The velocity is non-dimensionalized by the free stream velocity U. The elliptic cylinder has an aspect ratio AR $= a/b$, in which a and b are semi-major and semi-minor axes. The characteristic length is the major axis of the elliptic cylinder $D = 2a$. The non-dimensional temperature θ is defined as $\theta = \frac{T-T_\infty}{T_w-T_\infty}$, where T_w and T_∞ are the body temperature and the incoming flow temperature. The fluid properties such as density, thermal diffusivity, kinematic viscosity, and thermal expansion coefficient are denoted by ρ_f, κ, ν, and β, respectively. The pressure p is non-dimensionalized by $\rho_f U^2$. The Reynolds number Re $(= UD/\nu)$ is the ratio of the inertial force to the viscous force. The Richardson number Ri $(= g\beta\Delta\theta D/U^2)$ in Eq. (2) characterizes the importance of natural convection to the forced convection (Chang and Sa, 1990; Wan and Patnaik, 2016). When heat transfer is dominated by forced convection, the Richardson number is far below unity, i.e., $Ri \ll 1$; on the other hand, when heat transfer is dominated by natural convection, $Ri \gg 1$. The Prandtl number Pr in Eq. (3) is the ratio of the kinematic viscosity (momentum diffusivity) ν to the thermal diffusivity κ. Prandtl number is a property of the fluid medium only. In our study, water is considered and its Prandtl number is 7.1.

An elastically-mounted elliptic cylinder with one degree-of-freedom in x-direction (perpendicular to the free stream) is shown in Fig. 1. The vibration of an elastically mounted solid body in fluid can be described by the non-dimensional dynamics equation as follows:

$$\frac{d^2Q_x}{dt^2} + \frac{4\pi\zeta}{U_{red}}\frac{dQ_x}{dt} + \frac{4\pi^2}{U_{red}^2}Q_x = \frac{1}{2M_{red}}C_x \tag{4}$$

in which Q_x is the nondimensionalized (by the major axis) x-displacement of the body mass center with respect to the original position of the body centroid at rest. The reduced velocity U_{red} on the left hand side of Eq. (4) is defined as $U_{red} = \frac{U}{f_n D}$, where $f_n = \frac{1}{2\pi}\sqrt{k/m}$ is the natural frequency, and m and k are the mass and the spring stiffness of the solid body, respectively.

A flexible structure has smaller stiffness k, smaller frequency, and therefore higher U_{red}. Damping reduces the vibration amplitude and alters the response frequency of the structure (Newman and Karniadakis, 1997). In our study, the non-dimensional damping coefficient ζ is set to be zero to handle the worst scenario case.

Table 1
Grid convergence study using flow past a fixed cylinder at Re = 100.

$h = \Delta x = \Delta y$ (unit: D)	C_x	$\overline{C}_y$	St
0.02	0.319	1.334	0.164
0.015	0.322	1.340	0.165
0.01	0.322	1.341	0.165

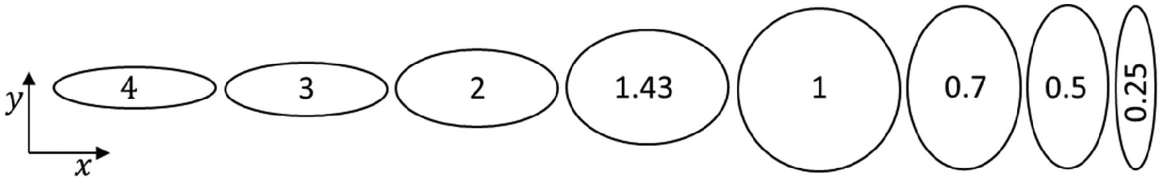

Fig. 2. Aspect ratios considered in the present study: 4, 3, 2, 1.43, 1, 0.7, 0.5, and 0.25.

On the right hand side of Eq. (4), C_x is the fluid force coefficient per unit length, i.e., $C_x = \frac{2F_x}{\rho_f U^2 D \cdot 1}$. The reduced mass $M_{red}(= \frac{m}{\rho_f D_h^2})$, denotes the mass ratio between the structure and displaced fluid, in which $m = \pi ab\rho_s$, and ρ_s is the density of the structure. D_h is the hydraulic diameter defined as $D_h = \frac{4ab\left(64-16E^2\right)}{(a+b)\left(64-3E^4\right)}$, where $E = \frac{a-b}{a+b}$. In our study, M_{red} is held constant at 10 to simulate a steel body in water.

3. Numerical method and simulation setup

3.1. Numerical method

The Navier–Stokes equations are discretized in time and space using a cell-centered, collocated arrangement in Cartesian grids. Finite volume method with second-order accuracy in space are employed to both convection and diffusion terms in momentum and energy equations. Immersed boundary method (Mittal and Iaccarino, 2005) is used identify the location and boundary of the body at each time instant. The Navier–Stokes equations are implicitly coupled with the body dynamics equation, and more details can be found in previous work (Wan et al., 2012a,b; Wan and Patnaik, 2016). The grid sensitivity study is carried out by varying the grid size in the refined mesh region, and the results of the amplitude of lift coefficient (C_x), time-averaged drag coefficient ($\overline{C}_y$), and Strouhal number ($St = \frac{Uf}{D}$) are listed in Table 1. The 0.015D grid is used in our simulations.

An in-depth grid convergence and validation analysis of the model can be found in our previous work (Wan and Patnaik, 2016). More validations were conducted in the present study against the simulation on free vibrations of elliptic cylinders of various aspect ratios (ARs) between 0.7 and 1.43 (Navrose et al., 2014). The corresponding results will be presented in Section 4.

3.2. Simulation setup

Simulations were conducted at $Re = 100$ and $M_{red} = 10$, at eight aspect ratios (ARs), as shown in Fig. 2. The VIV regimes, i.e., the lock-in and the flexible regions, need to be identified before considering heat transfer. The reduced velocity U_{red} is varied between 1 and 9 to cover both rigid and flexible stiffness.

Our simulations found that vortex induced vibration does not occur for AR = 0.5 and 0.25 within 1000 nondimensional time. This observation is consistent with the result from Kumar et al. (2018). Therefore, these two aspect ratios were eliminated from the further study. The aspect ratios AR = 0.7, 1 and 1.43 were selected to validate against literatures. The aspect ratio AR = 2, 3, and 4 extend beyond most available published literature to expand the knowledge base.

Table 2 shows the U_{red} values used to find the VIV regimes for each AR. For example, at AR 0.25, bodies with $U_{red} = 1$, 2, 3, 4, 5, 6, 7, 8, and 9 were simulated. At some aspect ratios, intermediate values of U_{red} were selected to add resolution to the data set.

Once the lock-in and unsynchronized regimes are identified for each aspect ratio, a U_{red} is selected in each region, as shown next to each AR in Table 3, in which Ri values used in search of critical Richardson number Ri_c are listed across the table at the given AR and U_{red}. Initially, six Ri are simulated between $Ri = 0.2$ and 1.2. Then intermediate test points are added to increase the resolution near where Ri_c appeared to be.

Recall that M_{red} is defined as $M_{red} = \frac{m_{body}}{\rho_f D_h^2}$, and $M_{red} = 10$ in our study, the density ratio corresponding to each aspect ratio is calculated and listed in Table 4. Since the aspect ratio 0.7 and 1.43 essentially have the same geometry, the density ratio is same in both cases.

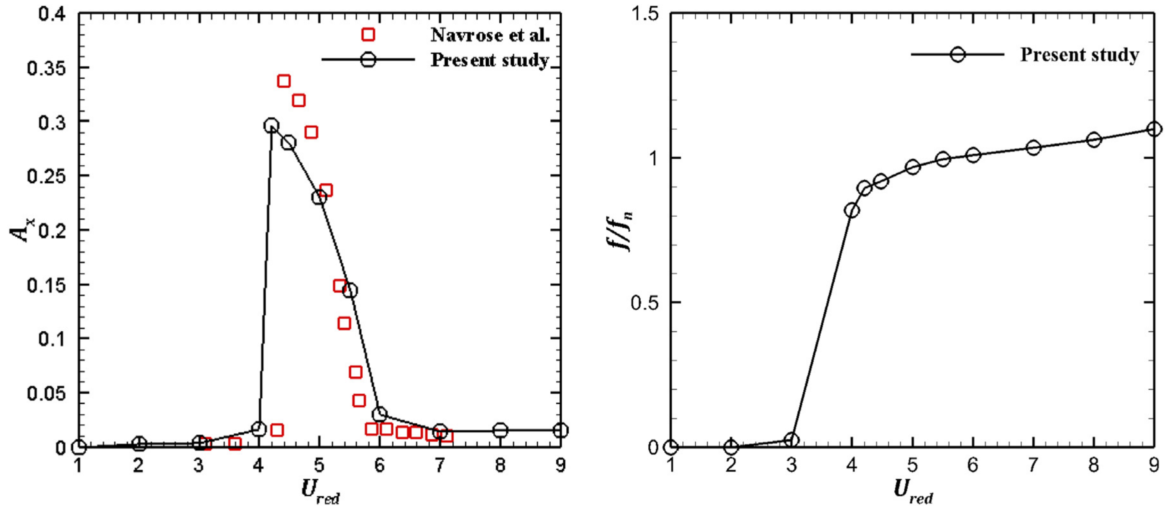

(a) Vibration amplitude (b) Frequency ratio

Fig. 3. U_{red} sweep for the cylinder of AR 0.7.

Table 2
U_{red} used to find VIV regimes for each considered AR.

AR	U_{red} values selected for each simulation; $Re = 100$, $M_{red} = 10$													
0.25	1	2	3	4	5	6	7	8	9					
0.5	1	2	3	4	5	6	7	8	9					
0.7	1	2	3	4	4.5	5	5.5	6	7	8	9			
1	1	2	3	3.5	4	4.5	5	5.5	6	7	8	9		
1.43	1	2	3	4	4.5	4.8	5	5.5	6	6.5	7	8	9	
2	1	2	3	3.5	3.8	4	4.5	5	5.5	6	7	8	9	
4	1	2	3	3.5	3.8	4	4.2	4.4	4.8	5	5.5	6	7	8	9

Table 3
Ri test points used to find Ri_c for each AR in the lock-in and unsynchronized regime.

AR	U_{red}	Ri values used to find Ri_c												
0.7	5	0.05	0.1	0.15	0.2	0.25	0.4	0.6	0.8	1				
	8	0.05	0.1	0.15	0.2	0.3	0.4	0.6	0.8	1				
1	5	0.2	0.25	0.28	0.3	0.35	0.4	0.45	0.5	0.6	0.8	1	1.2	
	8	0.1	0.15	0.2	0.25	0.3	0.4	0.6	0.8	1	1.2			
2	4.5	0.2	0.4	0.42	0.43	0.45	0.6	0.8	1	1.2				
	8	0.2	0.3	0.33	0.34	0.35	0.4	0.6	0.8	1.0	1	1.2		
3	4.5	0.2	0.4	0.8	0.88	0.9	0.91	0.92	0.95	0.97	1	1.2	1.2	
	8	0.2	0.4	0.8	0.9	0.92	0.93	0.94	0.95	0.96	0.97	1	1.2	
4	4.5	0.4	0.6	0.8	0.9	0.92	0.93	0.95	1.0	1.2	1.4	1.5	1.8	2
	8	0.4	0.6	0.8	0.9	1.0	1.2	1.4	1.45	1.5	1.6	1.7	1.8	2

4. Results and discussion

4.1. Overview

In the present study, an elastically-mounted rigid elliptic cylinder is allowed to oscillate in the transverse direction of the incoming flow. As shown in Fig. 1, a uniform flow enters from the bottom of the computational domain and exits from the top. The cylinder is subject to transverse vibrations in the x-direction as a result of vortex shedding. The cylinder is uniformly heated to a constant temperature to suppress the vortex-induced vibration (Wan and Patnaik, 2016).

Before the investigation of the temperature effect, we studied the vibration of non-heated cylinders of various aspect ratios at several reduced velocities. For each aspect ratio, we swept the reduced frequency to identify the lock-in region and the flexile region. As U_{red} increases, the natural frequency of the structure decreases. At each case, the non-dimensional oscillation amplitude A_x, the force coefficients C_x (transverse), C_y (drag coefficient), and vibration frequency are monitored to observe the structure response. The amplitude is the primary quantity used to determine the VIV regime. We then select

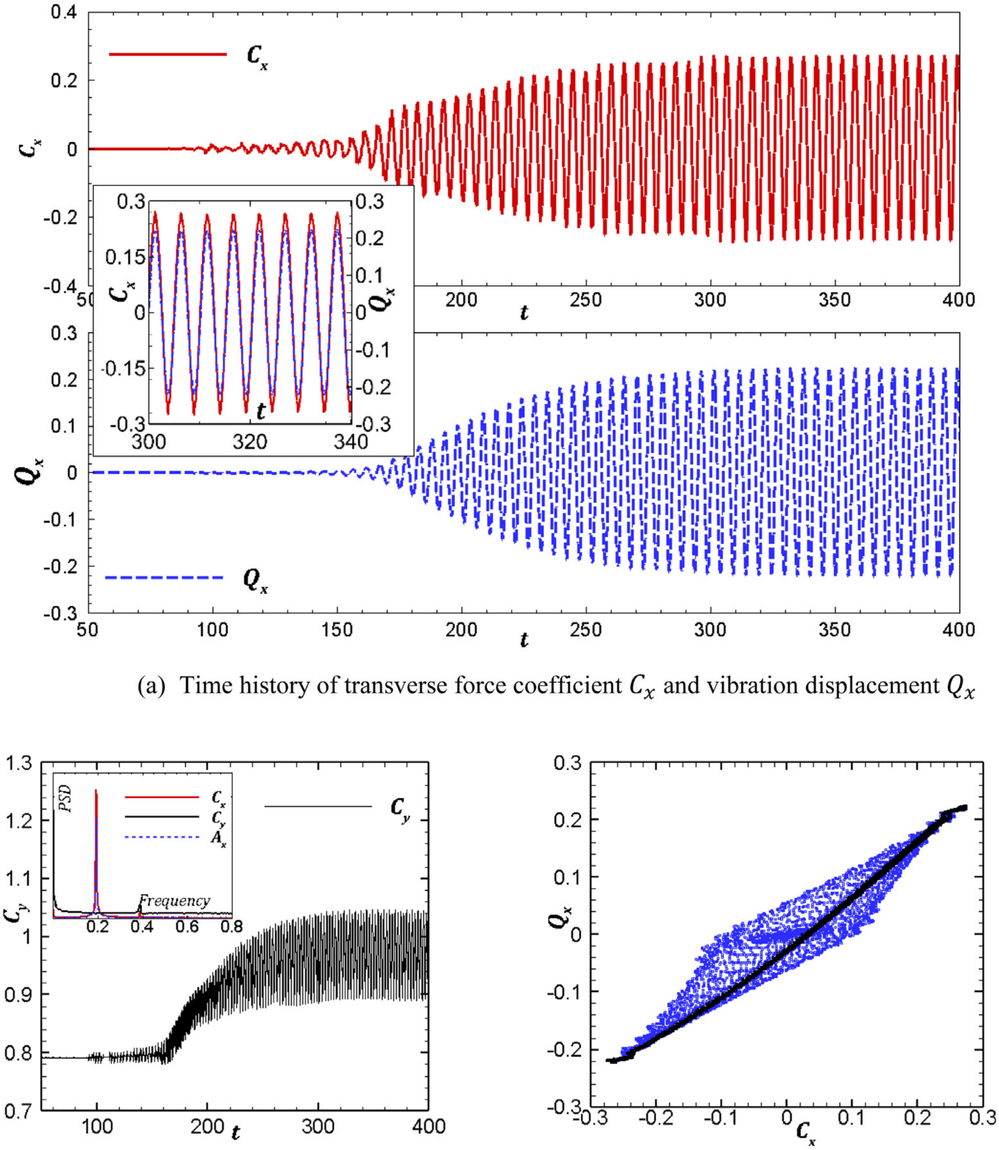

(a) Time history of transverse force coefficient C_x and vibration displacement Q_x

(b) Drag coeffiicent and PSD

(c) Phase plot

Fig. 4. AR = 0.7, lock-in region $U_{red} = 5$.

Table 4
Density ratio of cylinders with various aspect ratios.

AR	0.7	1	1.43	2	3	4
ρ_s/ρ_f	12.14	12.73	12.14	10.71	8.44	6.83

U_{red} in the lock-in and the flexible region, then increase the *Ri* to investigate the suppression of VIV and identify the critical Richardson number.

4.2. VIV of elliptic cylinders

4.2.1. **AR** = 0.7

At AR = 0.7, simulations of various reduced velocities were conducted. The amplitude and frequency at periodic vibration for each U_{red} are plotted in Fig. 3. The amplitude response starts with an initial branch in which U_{red} is small than 4 and the vibration amplitude A_x is small, followed by a lock-in (also called synchronization) region in which the

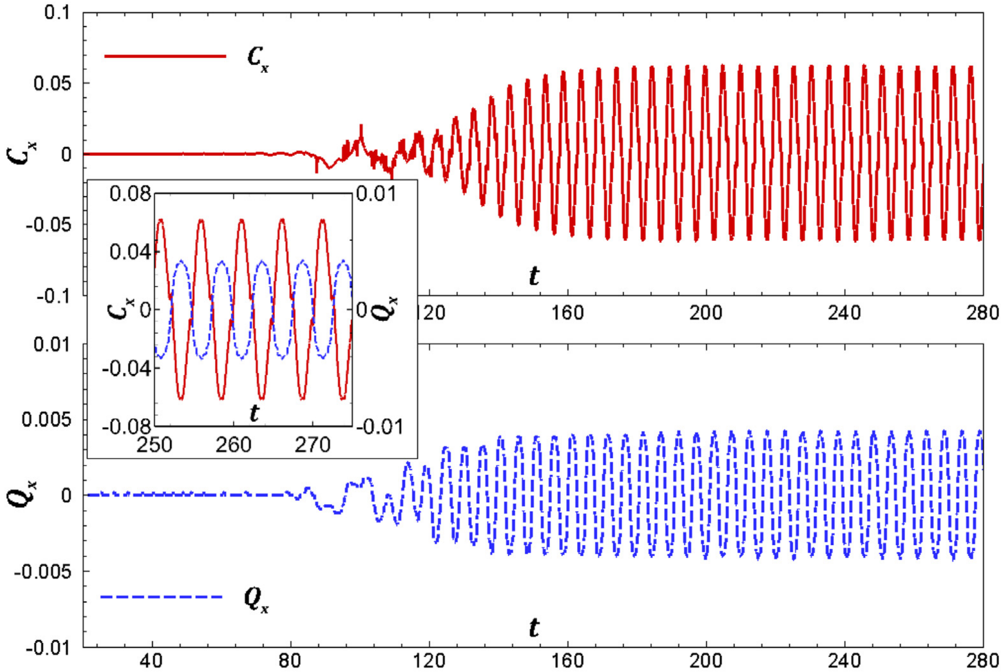

(a) Time history of transverse force coefficient C_x and vibration displacement Q_x

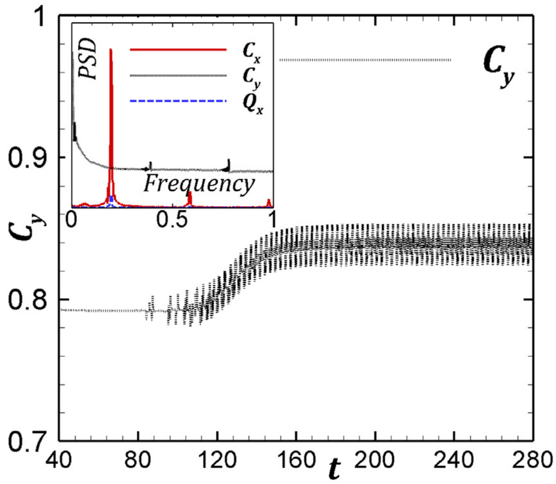

(b) Drag coeffiicent and PSD

Fig. 5. AR = 0.7, flexible region $U_{red} = 8$.

vibration amplitude is high. The amplitude is then reduced to 0.05 or even lower when U_{red} beyond 6, in which the vibration is called in the flexible region. Fig. 3(a) also shows the results from literature (Navrose et al., 2014), and the comparison on vibration amplitude is reasonably well. Navrose et al. used ramping of Re to study hysteresis; while Re was held at 100 in this study. Both simulations showed that the lock-in regime starts when U_{red} is slightly greater than 4, and the flexible region starts when U_{red} is greater than 6. Therefore, the lock-in region is $4 < U_{red} < 6$ for AR 0.7. The peak amplitude found in both studies is about $0.3D \sim 0.35D$, and the corresponding U_{red} is around 4.1. Fig. 3(b) shows f/f_n, the ratio between the body oscillation frequency and the natural frequency, in which $\frac{f}{f_n} \sim 1$ indicates the lock-in region where the body oscillates around its natural frequency.

Fig. 4(a) presents the time history of the force coefficient of a cylinder with AR = 0.7 and $U_{red} = 5$, at which the VIV is in the lock-in region and the transverse vibration displacement Q_x is high. The inset of Fig. 4(a) shows that Q_x and transverse force coefficient C_x oscillate in phase. The vibration amplitude of C_x is around 0.27. Fig. 4(b) shows the drag coefficient C_y, whose average is around 0.95. The inset in Fig. 4(b) shows the Fourier analysis of the force coefficients and

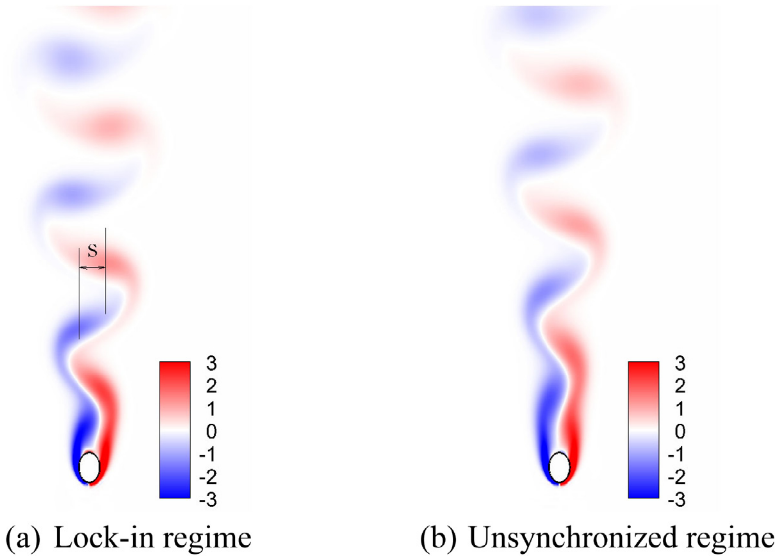

Fig. 6. Vorticity field of flow past a cylinder of AR = 0.7, in (a) lock-in regime and (b) unsynchronized regime.

the vibration amplitude, i.e., the power spectral density (PSD) versus the non-dimensional frequency. It shows that the dominant frequency of Q_x and C_x is around 0.19; and the oscillation frequency of C_y is 0.38. The phase plot composed of Q_x and C_x is shown in Fig. 4c. The blue dots show the transient process and the black dots show the periodic vibration. It can be seen that C_x and Q_x collapse on a straight line when the periodic vibration is reached, indicating C_x and Q_x oscillate in phase, which is consistent with their time history in Fig. 4a.

Fig. 5 presents the results of an elliptic cylinder with AR = 0.7 in the unsynchronized regime at which $U_{red} = 8$. The inset in Fig. 5(a) clearly shows that the transverse force and the displacement are out of phase. The vibration amplitude is only 0.004, which is two orders of magnitude smaller than that in the case of $U_{red} = 5$. Fig. 5(b) shows the drag C_y is 0.83 ± 0.03, i.e., the averaged drag $\overline{C}_y$ is 0.83, and the oscillation amplitude is 0.03. The inset in Fig. 5(b) shows the oscillation frequency of Q_x and C_x is around 0.19, and the oscillation frequency of C_y is around 0.38.

Fig. 6 shows the vorticity field of flow past an elliptic cylinder of AR = 0.7, in the lock-in regime (left) and the unsynchronized regime (right). Since the body is relatively thin and the vibration amplitude is small, the 2S mode vortex structure is generated in the wake, i.e., two alternate vortices are shed per cycle. It is similar to the classic von Kármán vortex street (Gabbai and Benaroya, 2005). Compared to the vortex structure in the wake of cylinders with wider aspect ratios, the vortex separation in the wake is small in both lock-in and unsynchronized regimes.

4.2.2. **AR** = 1

At AR = 1, U_{red} is varied from 1 to 9 to find the lock-in region. The amplitude and frequency ratio from the present study are shown in Fig. 7, as well as the results from Navrose et al. (2014). Both the amplitude and the width of the lock-in region fit well with the results of Navrose et al. (2014). The peak value of A_x between the two studies has 6.5% difference. The width of the lock-in region from Navrose et al. (2014) is wider than that from the present study. The reduced velocity U_{red} is varied by the change of the Reynolds number in Navrose et al. (2014); while U_{red} is directly varied as an independent control variable through the change of stiffness and the Reynolds number is fixed in the current study. The different way of varying U_{red} may lead to the different width of the lock-in region. It can be seen from the present study that the lock-in region is around $4.5 < U_{red} < 7.5$. The peak vibration amplitude is around 0.61 when U_{red} is 5. As U_{red} increases to 8, the vibration amplitude is smaller than 0.06. The frequency ratio in the lock-in region is close to unity. This provides an example of the peak lock-in value operating at a frequency ratio slightly offset from unity due to the added mass of the surrounding fluid (Sarpkaya, 2004).

Fig. 8 shows the results of flow past a cylinder with AR = 1 and $U_{red} = 5$. At $U_{red} = 5$, the body vibrates at the maximum amplitude. The phase diagram shows that the vibration displacement Q_x and C_x change in phase. The Fourier transform shows the frequency of C_x and Q_x is around 0.195, and the frequency of C_y is 0.392. The averaged drag $\overline{C}_y$ is 2.21, and the oscillation amplitude of C_y is around 0.73. Fig. 8(C) presents the phase plot of Q_x and C_x, in which the blue and black dots represent the transient and periodic vibration, respectively. A figure-8 shape of phase plot is presented when periodic vibration is reached in the case of AR = 1 and $U_{red} = 5$.

Fig. 9 shows that the forces and vibration displacement of an AR = 1 cylinder in unsynchronized regime, $U_{red} = 8$. The negative correlation between the displacement and force coefficient C_x may be determined. The mean drag coefficient $\overline{C}_y$ is 1.29, substantially lower than the mean drag coefficient value 2.21 in the case of $U_{red} = 5$.

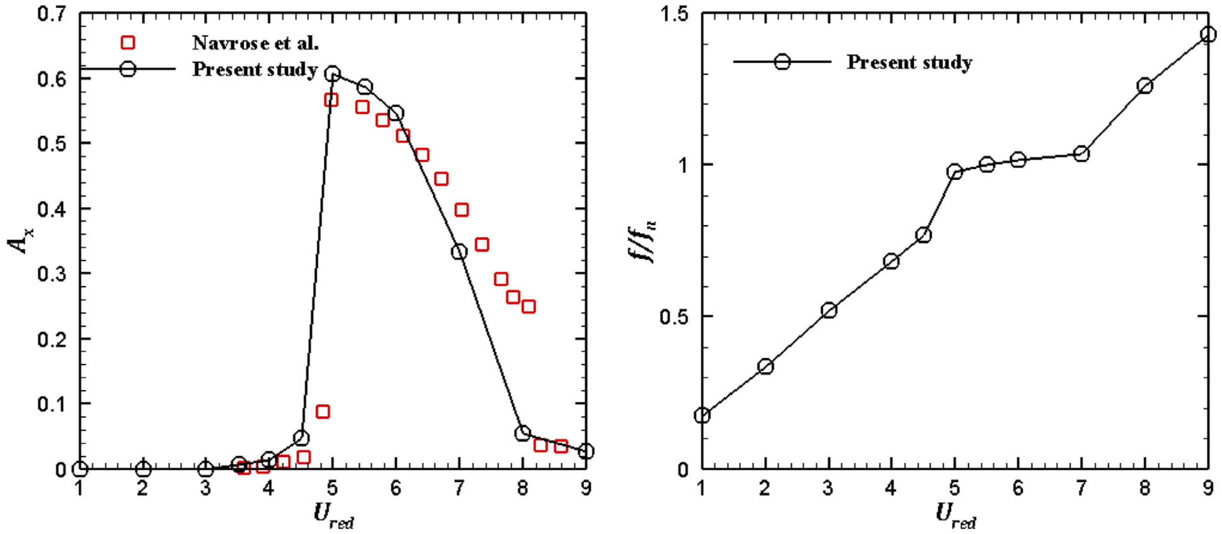

(a) Vibration amplitude (b) Frequency ratio

Fig. 7. U_{red} sweep results for AR = 1. (a) Vibration amplitude in comparison with Navrose et al. (2014); and (b) frequency ratio from the present study.

The vortex structure is presented in Fig. 10 for flow past an AR = 1 cylinder. It can be seen that two-column vortices were shed from the body in the lock-in region. The separation between the two columns is about 1.5D, which is greater than that generated by flexible AR = 0.7 cylinder. For the AR = 1 cylinder in unsynchronized regime, typical 2S vortex street is obtained.

4.2.3. **AR** = 1.43

At AR = 1.43, the vibration amplitude and frequency responses to various U_{red} are shown in Figs. 11a and 11b.

Fig. 12 presents the force coefficients at $U_{red} = 5$. The inset in Fig. 12(a) shows that the displacement Q_x and corresponding transverse force oscillate out-of-phase, which is different from the case of AR = 1 in the lock-in regime (Fig. 8). The amplitude of VIV is 0.67. The time-averaged drag coefficient , $\overline{C}_y$ is 2.62, and the oscillation amplitude of C_y is 0.97.

The force coefficients and phase diagram of body in flexible region ($U_{red} = 8$) are shown in Fig. 13. The phase diagram shows that the displacement and force are out of phase. The vibration amplitude is 0.09. For cylinder with aspect ratio 1.43, $\overline{C}_y$ reduces from 2.62 in lock-in regime to 1.56 in the unsynchronized regime, since the higher drag coefficient associates with higher body displacement.

The flow visualization in Fig. 14 shows the vortex structure of flow past cylinders of aspect ratio 1.43. Again, two-column vortex structure is developed for the case of lock-in region, where the separation S is around 1.7*D*. Recall the separation of the two-column vortices developed by lock-in AR = 1 cylinder is around 1.5*D* (Fig. 10), it shows that the separation gets wider as the aspect ratio increases. For the cylinder in unsynchronized regime, the von Karman vortex street is obtained (Fig. 14b).

The three ARs from 0.7, 1, to 1.43 conclude the comparison and validation of the present study against the study of Navrose et al. (2014). In the current study, U_{red} is changed by varying the stiffness of the structure, while *Re* is fixed 100. In Navrose et al. (2014), *Re* was varied from 60 to 140 to alter U_{red}. Even though U_{red} is changed in different ways, the two studies generated similar results of VIV amplitude and the range of lock-in region.

4.2.4. **AR** = 2 *and* **AR** = 4

Fig. 15 shows the periodic vibration amplitude and frequency ratio versus U_{red} of the cylinders with AR = 2 and AR = 4. The amplitude plot from Fig. 15 clearly shows the upper branches widening from $3 < U_{red} < 4$ for AR = 2 to about $2.5 < U_{red} < 4.2$ for AR = 4. At $U_{red} = 8$. The VIV amplitude in lock-in region increases from approximately 0.9 for AR = 2 to 1.1 for AR = 4. At higher aspect ratio, the frequency ratio is essentially unity at the peak amplitudes, the resonance frequency is essentially the natural frequency in the vacuum.

Fig. 16(a) shows Q_x and transverse force coefficient C_x in both transient and steady vibration of a cylinder with AR = 2 and reduced velocity $U_{red} = 4.5$. From the inset, it can be seen that the force and the displacement oscillate in phase. Fig. 16(b) shows the transient response of the drag coefficient C_y and the power spectral density (PSD) analysis on the force and vibration displacement. The averaged drag coefficient is 3.48 and its oscillation amplitude is 1.49. The frequency

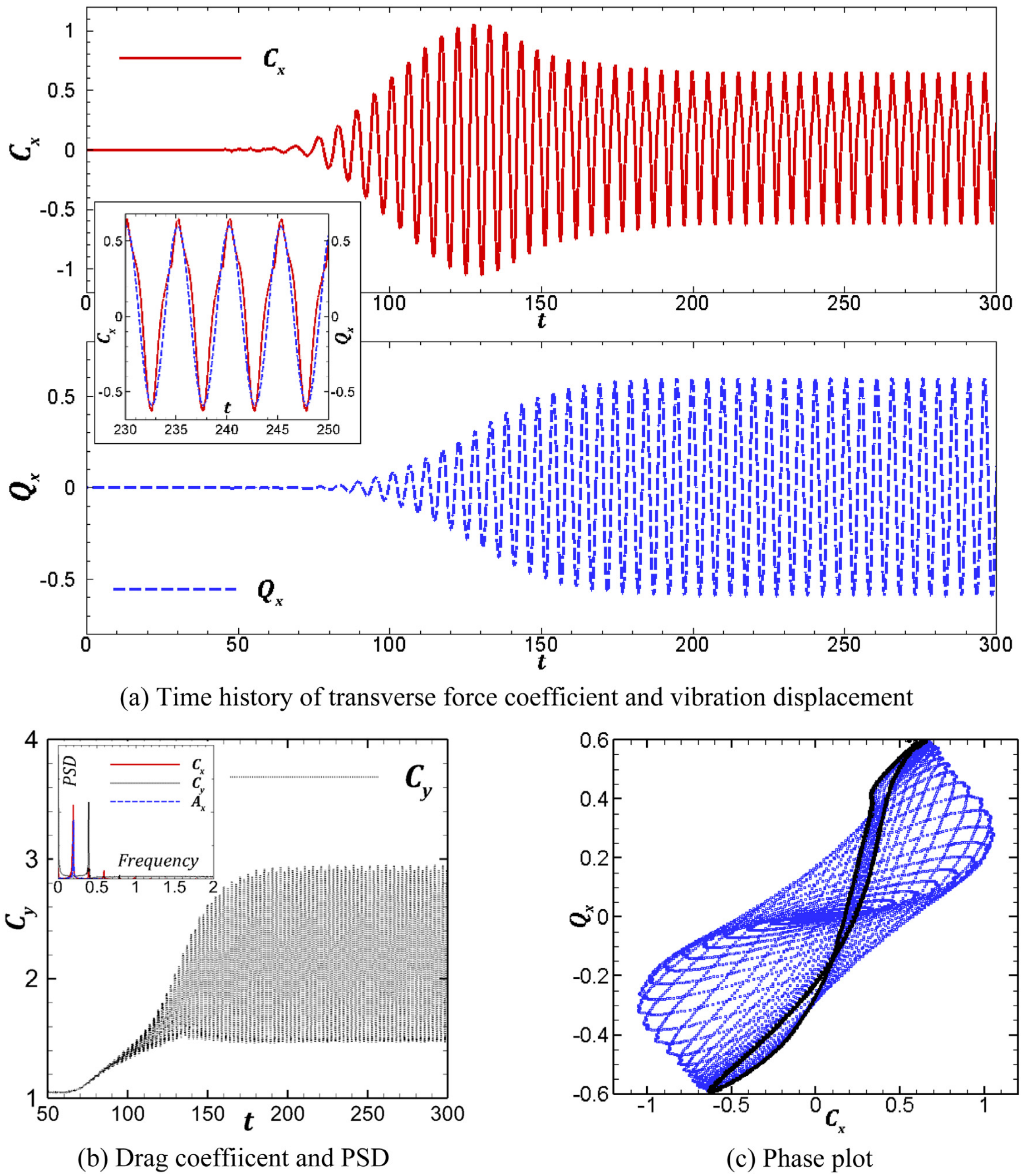

(a) Time history of transverse force coefficient and vibration displacement

(b) Drag coeffiicent and PSD

(c) Phase plot

Fig. 8. Cylinder of AR = 1 in lock-in region, $U_{red} = 5$.

of C_x and Q_x is 0.22, and the frequency of C_y is 0.44. The phase diagram in Fig. 16(c) composed of the lift coefficient and the displacement shows a figure-of-eight shape.

Fig. 17(a) shows Q_x and transverse force coefficient C_x in both transient and steady vibration of a cylinder with AR = 2 and reduced velocity $U_{red} = 8$. The force and the displacement oscillate in opposite phase. Fig. 17(b) shows the transient response of the drag coefficient C_y and the power spectral density of the force and vibration displacement. The drag coefficient C_y is around 1.85 ± 0.08. The frequency of C_x and Q_x is 0.18, and the frequency of C_y is 0.36. The phase plot in Fig. 17(c) shows that C_x and Q_x oscillate in opposite phase.

Fig. 18(a) shows Q_x and transverse force coefficient C_x in both transient and steady vibration of a cylinder with AR = 4 and reduced velocity $U_{red} = 4.5$. Again, the force and the displacement oscillate in phase. Fig. 18(b) shows the transient response of the drag coefficient C_y and the PSD of the force and vibration displacement. The averaged drag coefficient is 4.21 and the vibration amplitude is 1.41. The fundamental frequency of C_y and Q_x is 0.44, and 0.22, respectively. The

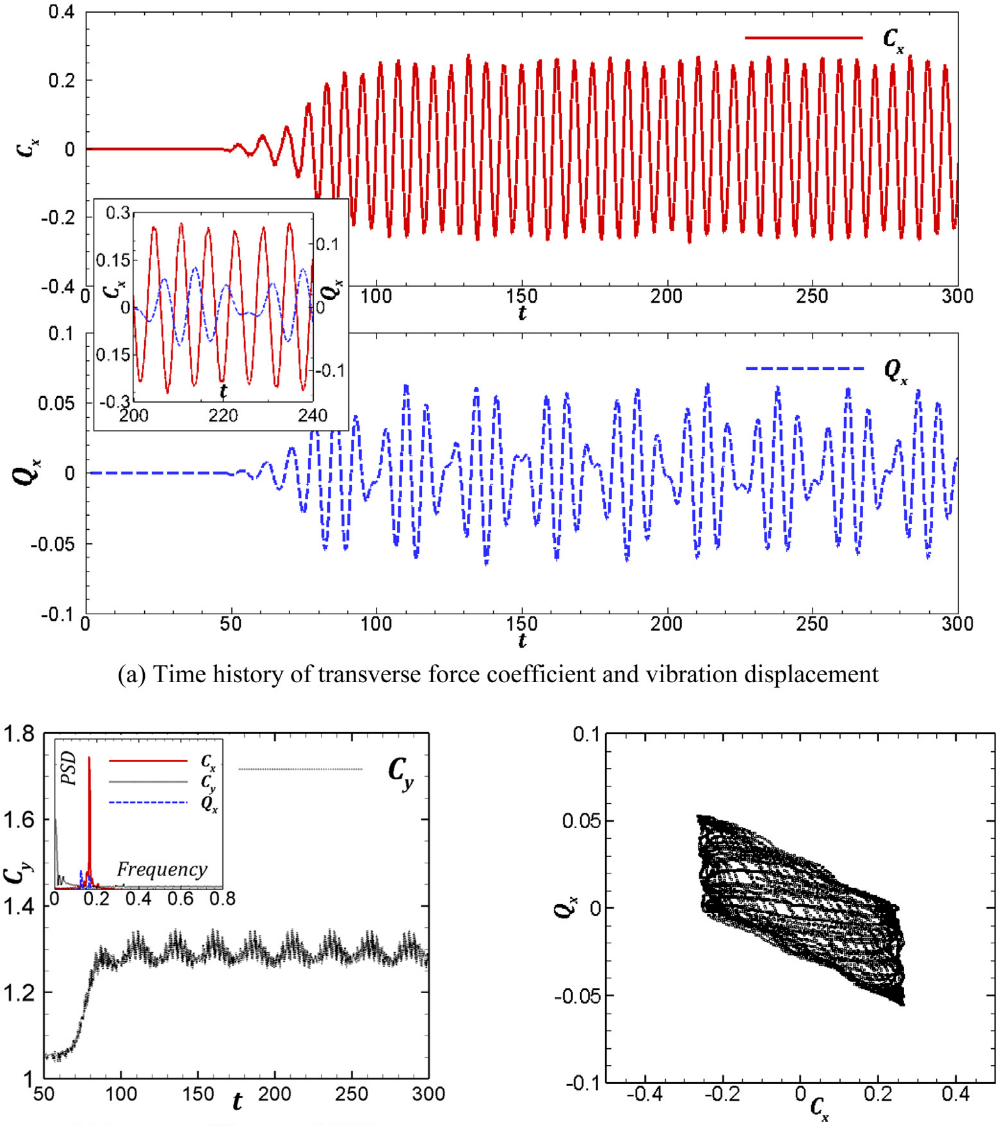

(a) Time history of transverse force coefficient and vibration displacement

(b) Drag coeffiicent and PSD

(c) Phase plot

Fig. 9. Cylinder of AR = 1 in flexible region, $U_{red} = 8$.

frequency of C_x with highest PSD is 0.22, followed by 0.66 and 0.44. In Fig. 18(c), the phase diagram shows a shape of figure-of-eight, as in the previous case of AR = 2 and $U_{red} = 4.5$.

Fig. 19(a) presents Q_x and transverse force coefficient C_x in both transient and steady vibration of a cylinder with AR = 4 and reduced velocity $U_{red} = 8$. It can be seen that the force and the displacement oscillate in opposite phase. Fig. 19(b) shows the transient response of the drag coefficient C_y and the PSD of the force coefficient and VIV displacement. The drag coefficient C_y is around 2.47 ± 0.28 in periodic oscillation. The fundamental frequency of C_x and Q_x is 0.19, and the fundamental frequency of C_y is 0.38.

The flow visualization in Fig. 20 shows the vortex structure of flow past body with aspect ratio 2 in lock-in and unsynchronized regimes. The transverse separation between the two vortex columns is around 4D for the cylinder in lock-in regime. Since there two alternate vortices are shed in each vibration cycle and the separation between them is wide, we therefore denote this vortex structure as W2S in Table 5 to differentiate it from typical 2S. Similar vortex structure was also found in the study of Wang et al. (2019) on AR 2 cylinder in the lock-in regime. The vortex structure of AR 2 cylinder in the unsynchronized regime is still the typical 2S, as shown in Fig. 20(b).

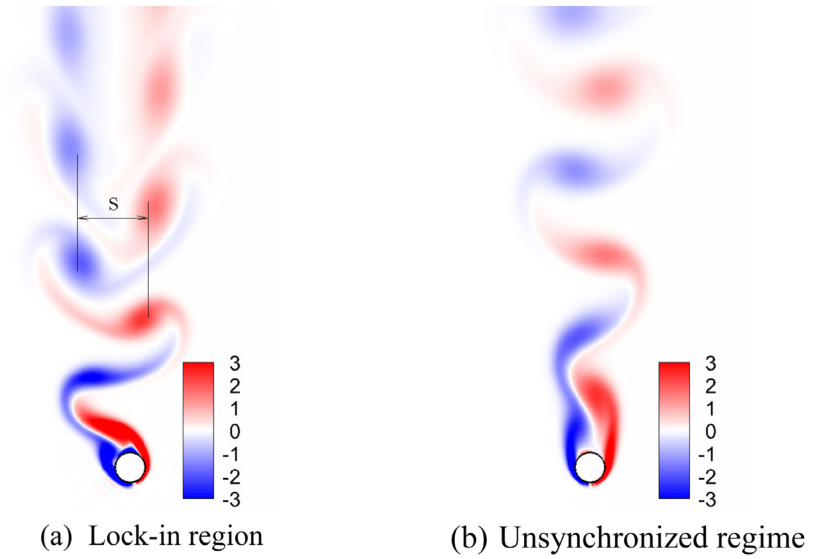

Fig. 10. Vortex structure in (a) the lock-in regime and (b) the unsynchronized regime. The vortex separation, S, is approximately 1.5*D* for the lock-in regime.

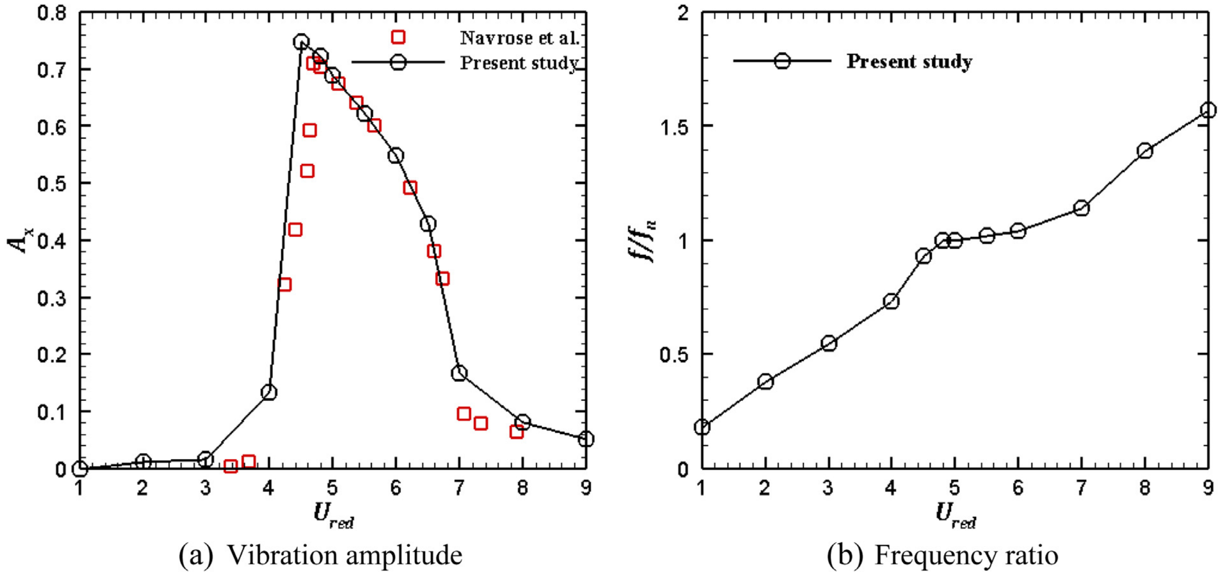

Fig. 11a. The lock-in region is around $4.5 < U_{red} < 6$. The peak amplitude in the lock-in region is about 0.75, and the corresponding frequency ratio is slightly less than unity.

The vortex structure of flow past AR 4 cylinder is shown in Fig. 21. In lock-in regime, the separation between the two vortex columns is around 4.3*D*, which is higher than that of AR 2 bodies. It is worth to note that for the AR = 4 cylinder, even in unsynchronized regime, the vortices also have two-column structure, with a separation of around 3*D*.

Table 5 summarizes the vibration amplitude, the force coefficients, the phase plot consists of the transverse displacement and transverse force, and the wake vortex structure of various elliptic cylinders. As expected, the vibration amplitude A_x, the amplitude of the transverse force coefficient C_x, and the mean drag coefficient $\overline{C}_y$ continues to increase as AR increases for VIV in both lock-in and flexible regions. The vortex structure in the wake is either 2 S or W2S, with the latter denoting the wide transverse distance between the two columns of the alternate vortices.

For VIV in lock-in regime, the VIV displacement, Q_x, varies with C_x in-phase, except the AR 1.43 cylinder. The phase portrait is a straight line for small AR, and becomes figure-8 for AR equal or greater than 1. For AR 1.43 cylinder, Q_x varies out-of-phase with C_x, this phenomena was also mentioned in the study of Navrose et al. (2014), due to the phase jump in the lock-in regime.

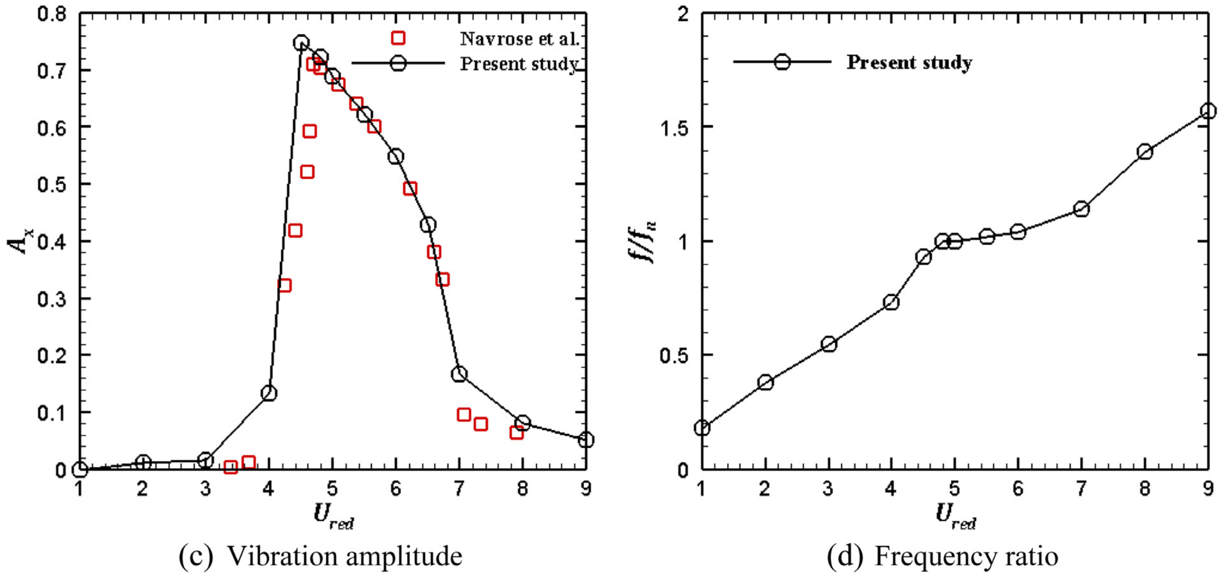

Fig. 11b. U_{red} sweep for AR = 1.43. (a) Vibration amplitude in comparison with Navrose et al. (2014); and (b) frequency ratio from the present study.

Table 5
VIV properties of elliptic cylinders with various aspect ratios.

AR	Lock-in regime (U_{red} = 4.5, 5)					Unsynchronized regime (U_{red} = 8)				
	A_x	C_x Amp	$\overline{C}_y \pm$ Amp	Phase plot[a]	Wake	A_x	C_x Amp	$\overline{C}_y \pm$ Amp	Phase plot[a]	Wake
0.7	0.22	0.27	0.95 ± 0.08	+ Line	2S	.004	0.06	0.83 ± 0.03	−	2S
1	0.60	0.63	2.21 ± 0.73	+ Figure-8	2S	0.06	0.25	1.29 ± 0.04	− Envelope	2S
1.43	0.67	0.37	2.62 ± 0.97	− Figure-8	2S	0.09	0.41	1.56 ± 0.09	− Envelope	2S
2	0.90	0.47	3.48 ± 1.49	+ Figure-8	W2S	0.095	0.51	1.85 ± 0.08	− Line	2S
4	1.08	0.25	4.21 ± 1.41	+ Figure-8	W2S	0.26	0.53	2.47 ± 0.28	− Line	W2S

[a]Phase plot between force (C_x) and displacement (Q_x): +denotes in-phase; −denotes out-of-phase.

For VIV in unsynchronized regime, the phase between Q_x and C_x is opposite for the studied elliptic cylinders. The vibration amplitude of AR 0.7 cylinder is only around 0.4%. Hence, it does not show an obvious pattern in the phase plot. For AR 1 and AR 1.43 cylinders, phase portrait is confined within a bounded envelope, instead of forming a closed trajectory. For AR 2 and AR 4 cylinders, C_x and Q_x is out-of-phase and forms a synchronized straight line.

Note for AR 4 cylinder, even though the VIV displacement Q_x responses to C_x in a very different way in the two regimes, one being indicated as in-phase figure-8 in the lock-in regime, the other being out-of-phase straight line synchronization in the unsynchronized regime, both regimes generate the same vortex structure, i.e., the two column vortices with wide separation (W2S). Therefore, we will use AR 4 as an example to analysis the variation of vortex structure when thermal effect is considered.

4.3. VIV suppression using thermal effect

The VIV of elliptic cylinders with various aspect ratios has been characterized in the previous section, the thermal effects on VIV suppression are now investigated. For each cylinder, one U_{red} is selected for the lock-in regime, and one for the unsynchronized regime (Table 3), respectively. The Richardson number is swept to investigate the thermal effect on VIV. Based on the study in the previous section, we know that the maximum VIV is generated by the cylinder with aspect ratio 4. Hence, we will focus on the suppression of VIV for the cylinder of AR 4.

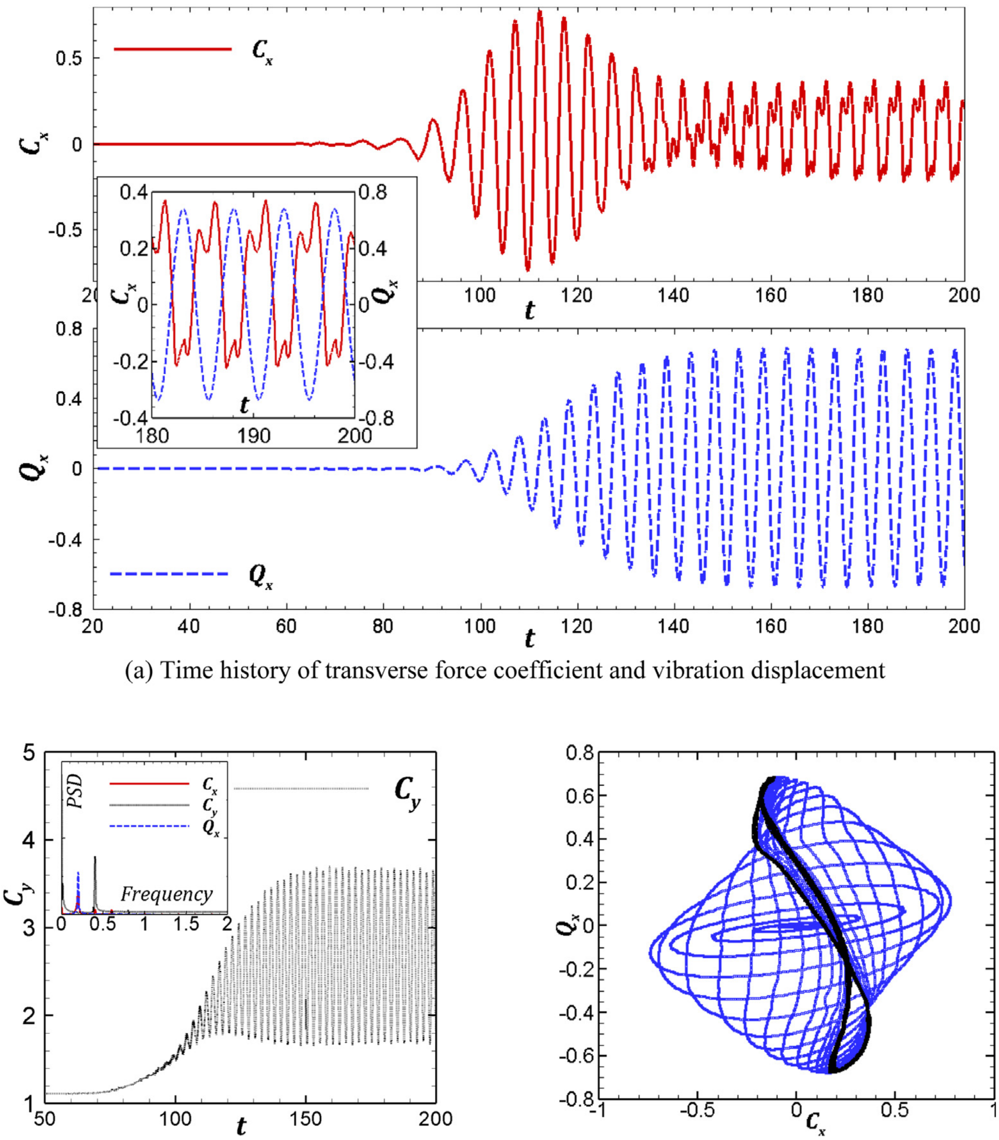

(a) Time history of transverse force coefficient and vibration displacement

(b) Drag coeffiicent and PSD

(c) Phase plot

Fig. 12. Cylinder of AR = 1.43 in lock-in region, $U_{red} = 5$, $C_y = 2.62 \pm 0.97$.

4.3.1. Suppression of VIV in lock-in regime

Fig. 22 shows the variation of the vortex structure as Ri increases for a cylinder with $M_{red} = 10$, and $U_{red} = 4.5$. At $Ri = 0.4$, the wake shows the W2S vortex structure. At $Ri = 0.8$, the W2S vortex structure still exist, especially in the near field of the wake. The separation between the two vortex columns is decreased though. As Ri is increased to 0.93, which is the critical Richardson number Ri_c in this case, the vortex shedding is fully suppressed, and the vortices in the near field are attached to the aft body.

The temperature field of flow past the AR = 4 cylinder at the critical Richardson number 0.93 is shown in Fig. 23(a). Since VIV is fully suppressed, the temperature field is symmetric around the centerline of the body. The vorticity contour lines and velocity vector at various downstream sections are presented in Fig. 23(b), in which the solid and dash lines represent the positive and negative vorticity, respectively. The vorticity contour is symmetric with respect to the body centerline. The two attached vortices in the flow reverse region can be clearly seen. In the near field of the wake, such as at the section 0.5D downstream of the body, the velocity vector indicates that there exists a strong reverse flow region, induced by the vortices attached to the body. At section 1.5D, the velocity deficit region gets narrower. At section 3D, out of the region of the attached vortex, the velocity is pretty much recovered, with only a little deficit region near the

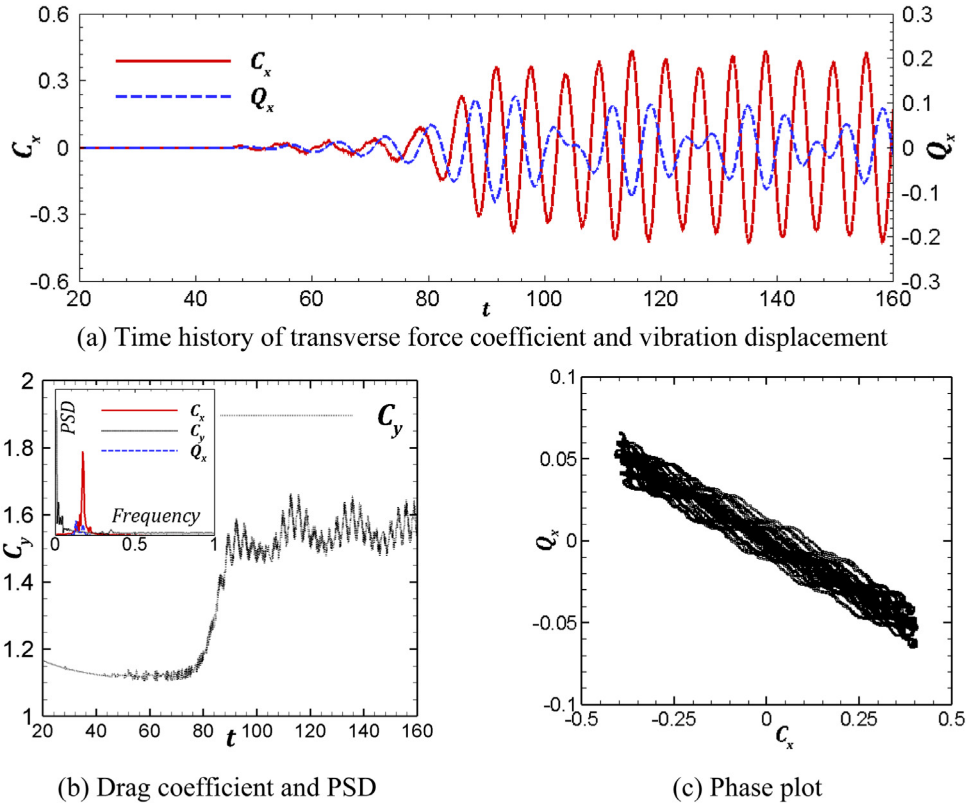

Fig. 13. Cylinder of AR = 1.43 in flexible region $U_{red} = 8.C_y = 1.56 \pm 0.10$.

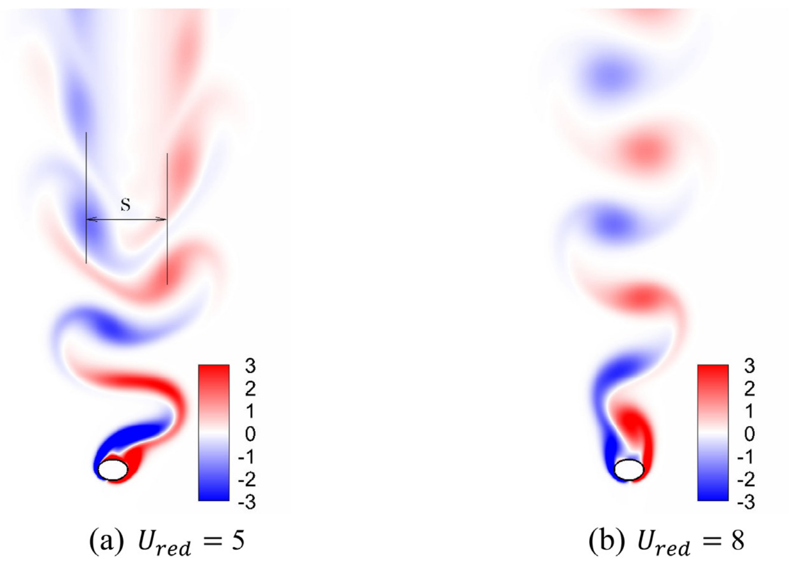

Fig. 14. Vorticity field when flow past a cylinder of AR = 1.43 in (a) lock-in regime and (b) unsynchronized regime. The vortex separation, S, is approximately 1.7D in the lock-in regime.

centerline. At the far field such as the section 10D, compared to the incoming uniform flow, the velocity at the centerline is actually higher, due to the thermal induced buoyancy force.

To further understand the thermal effects on the velocity, especially the vertical component v, we present in Fig. 24 the 10-period time-averaged $v-$ component field, for Ri at 0, 0.6, 0.8, and 0.93. The averaged location of the elliptic cylinder is

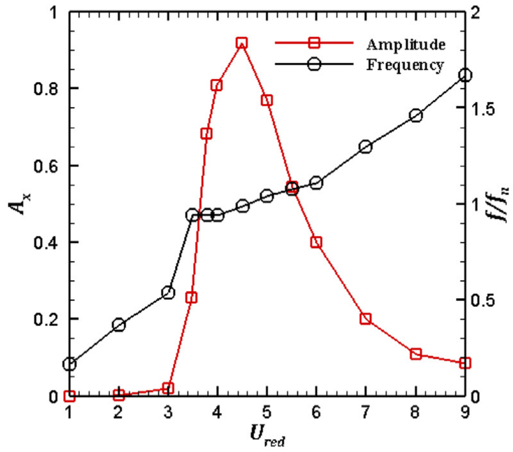

(a) AR = 2

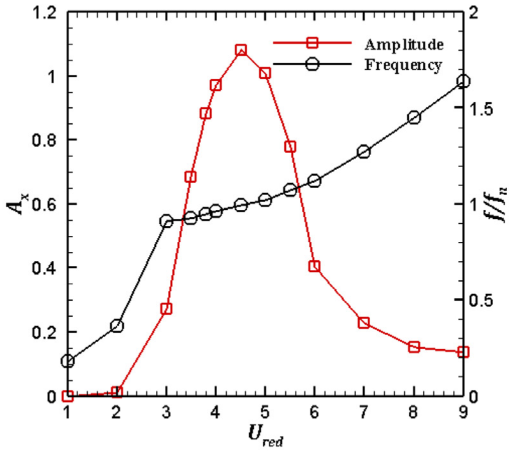

(b) AR = 4

Fig. 15. U_{red} sweeping results for AR = 2 and AR = 4.

Table 6
Summary of critical Richardson number Ri_c and time averaged drag coefficient $\overline{C}_y$ for cylinders in lock-in regime. $Re = 100$, $Pr = 7.1$, $M_{red} = 10$.

AR	U_{red}	Ri_c	$\overline{C}_y$ at $Ri = 0$	$\overline{C}_y$ at Ri_c	$\overline{C}_y$ reduction (%)
0.7	5	0.20	0.95	0.92	3.16
1	5	0.25	2.21	1.38	37.5
2	4.5	0.43	3.48	1.73	50.2
3	4.5	0.91	3.92	2.27	42.1
4	4.5	0.93	4.21	2.42	42.8

also outlined. In Fig. 24(a)–(c), the velocity unity is denoted by white color, which demarcates the velocity deficit region. At $Ri = 0$, we can see in the wake a wide velocity deficit region, and its width further increases when goes downstream. At $Ri = 0.6$ and 0.8, the velocity deficit region gets narrower, compared to the case of $Ri = 0$. Especially, the velocity deficit region converges in the far field when $Ri = 0.8$. The averaged v-component in Fig. 24(a)–(c) is above zero, indicating that there is no reverse flow region in the field, in the sense of time-averaged. At the critical Richardson number 0.93, as shown in Fig. 24(d), we can see a small velocity deficit region in the near wake. Also, there exists a reverse flow region above the cylinder (also shown in Fig. 23(b)). In the far field of the wake, we can see a velocity enhancement region across the centerline. The time-averaged velocity component v along the centerline is presented in Fig. 25, in which $y = 0$ is the center of the cylinder. Hence, $y > 0$ is the downstream region. At $Ri = 0$ and 0.6, v along the centerline decreases monotonically. At $Ri = 0.8$, v decreases along the centerline, until around 10 body-length in the downstream, then v starts to gradually increase. For all these three cases, v is less than 1, indicating that the region along the centerline is the velocity deficit region. At $Ri = 0.93$, the cylinder is stationary since the vibration is suppressed, as indicated by the plateau near $y = 0$. In the downstream until y is around 1.5, we see a reverse flow region, since v is negative. The magnitude of the maximum reverse velocity is around 40% of the incoming flow. As y in the range from 1.5 to 3.5, v is positive but smaller than the incoming flow velocity. Hence, this is a velocity deficit region. As y further goes into downstream, v is greater than the unity velocity and a velocity jet is formed afterwards. This change of velocity v in the wake gives rise to the drag reduction (Wan and Patnaik, 2016).

Table 6 lists the U_{red} in the lock-in regime, Ri_c, mean drag coefficient at $Ri = 0$ and Ri_c, for the studied elliptic cylinders. The drag reduction percentage is listed in the last column. The reduction of time-averaged drag can be approximately 40% or even higher for ARs greater than or equal to 1. The maximum reduction was around 50.2% for AR = 2. The minimum reduction was found to be only 3.16% for AR = 0.7.

4.3.2. Suppression of VIV in unsynchronized regime

Fig. 26 shows the variation of the vortex structure as Ri increases for a cylinder with $M_{red} = 10$ and $U_{red} = 8$. At $Ri = 0.4$, the wake is the typical 2S vortex structure. At $Ri = 1.5$, which is the critical Richardson number Ri_c, the vortex shedding is suppressed, with the vortices in the near field attached to the aft body. At $Ri = 1.0$ and 1.4, typical 2S vortex structure is formed in the near field of wake. However, as transporting further into the downstream, the vortices tend to across the centerline and form a crossed-2S vortex structure, as shown in Fig. 26(b) and (c). The red and blue dash lines indicate the trajectory of the positive (red) and negative (blue) vortices, respectively. For example, the positive vortices in Fig. 26(b) are initially generated at the right edge of the elliptic cylinder and advected into downstream region. After

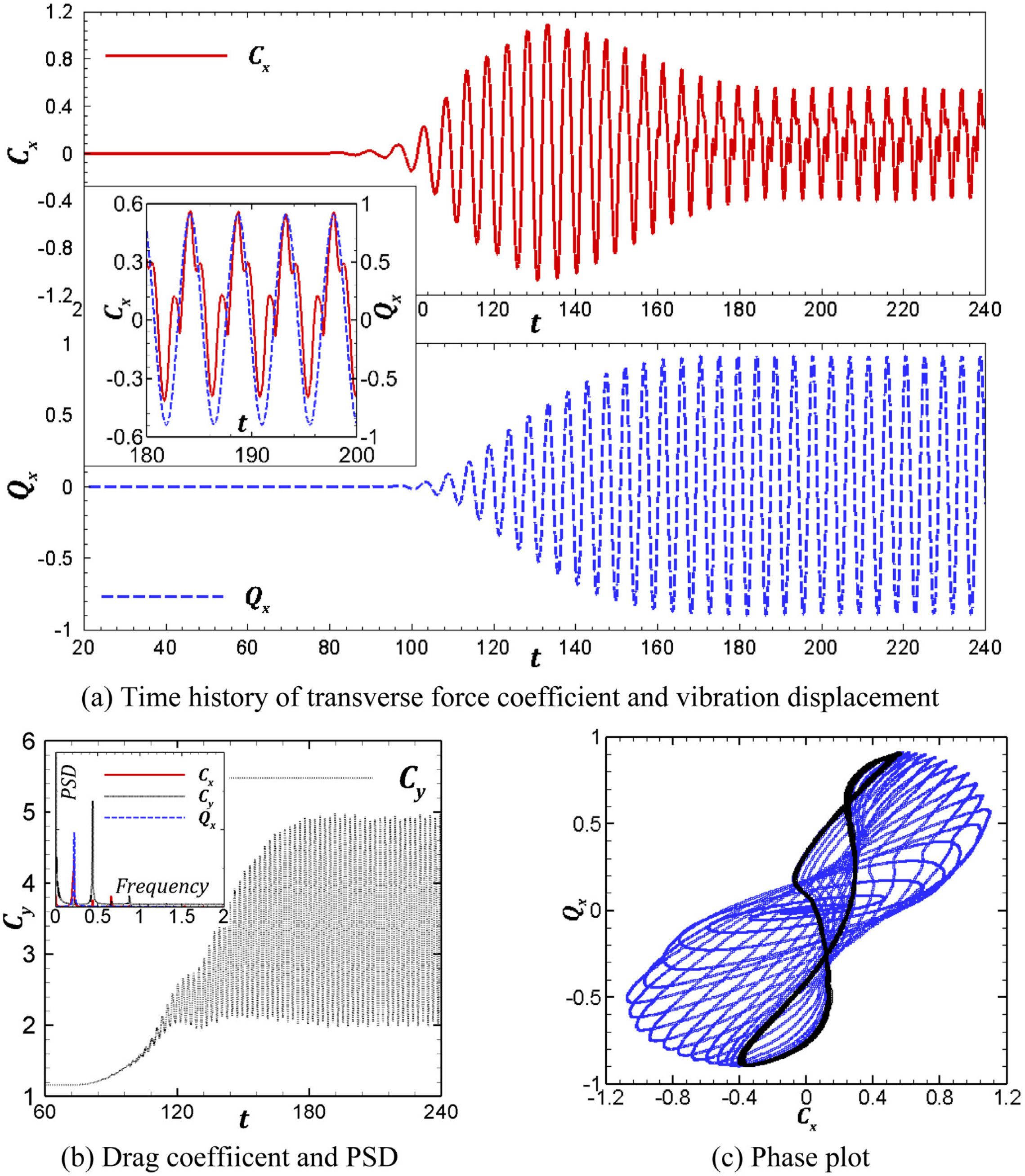

Fig. 16. Cylinder of AR = 2 in lock-in regime, $U_{red} = 4.5$.

three vibration cycles, the positive vortices crossed the centerline. When Ri increases to 1.4, as shown in Fig. 26(c), the vortices only take two vibration cycles to across the centerline, and the angle between the two dash lines gets bigger.

The time-averaged vertical velocity component v and the location of the elliptic cylinder are presented in Fig. 27 for the cases of $Ri = 0$, 0.4, 1.0, and 1.5. At $Ri = 0$, we can see the velocity deficit region is narrower in unsynchronized regime than that in lock-in regime, since the vibration amplitude is smaller in the unsynchronized regime. At $Ri = 0.4$, the velocity deficit region is narrower and the magnitude is weaker, compared to the case of $Ri = 0$. At $Ri = 1.0$, the velocity deficit is localized in a region within 5 body-length, beyond which a velocity enhancement region is gradually developed along the centerline. At critical Richardson number 1.5 (Fig. 27d), we can see an even smaller velocity deficit region in the near wake and a velocity enhancement region in the far field across the centerline.

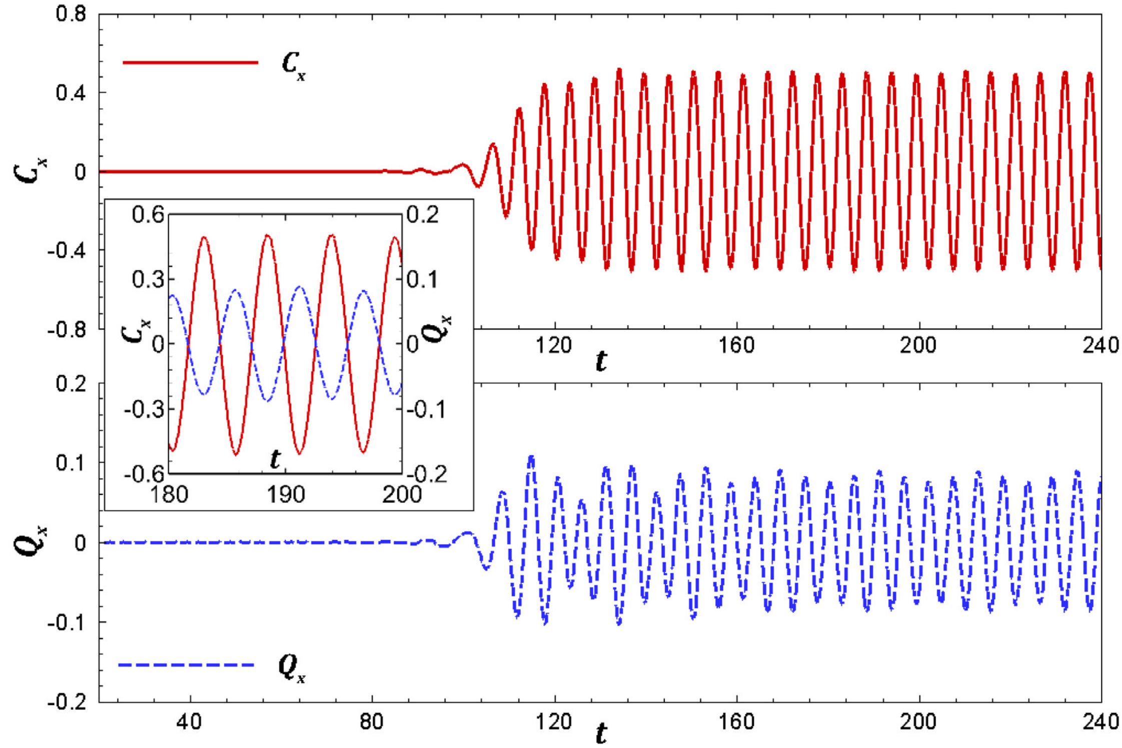

(a) Time history of transverse force coefficient and vibration displacement

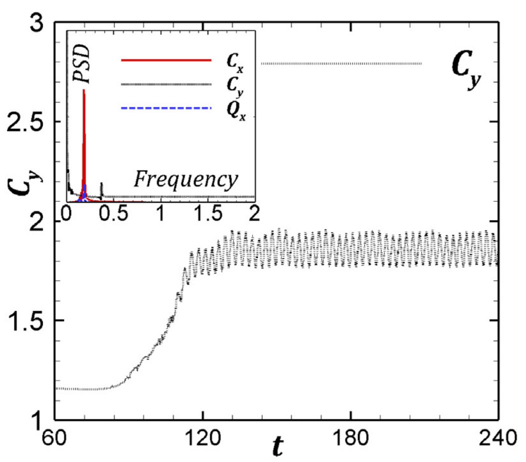

(b) Drag coeffiicent and PSD

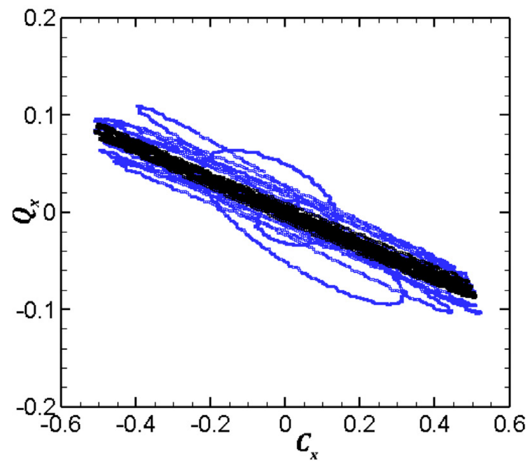

(c) Phase plot

Fig. 17. Cylinder of AR = 2 in unsynchronized regime, $U_{red} = 8$.

The time-averaged velocity component v along the centerline for the selected *Ri* is presented in Fig. 28. Since the amplitude of VIV is small in the unsynchronized regime, flow in the upstream is weakly disturbed. Therefore, v drops to a value close to zero and the profile in the upstream is pretty much overlapped to each other for various *Ri*. In the downstream, at $Ri = 0$, v increases to 0.4 at $y = 1$ along the centerline, then v decreases in far field. At $Ri = 0.4$, v pretty much increases as the flow goes further downstream, due to the thermal generated buoyancy effect. However, v is still below the incoming flow velocity. At $Ri = 1.0$, v increases from $y = 0$, and v is above 1 once y is beyond 5 body-length.

At $Ri_c = 1.5$, the vibration is suppressed. A reverse flow region exists in the downstream region up until y is around 1.2, within which v is negative. The magnitude of the maximum reverse velocity is about 40% of the incoming flow. A

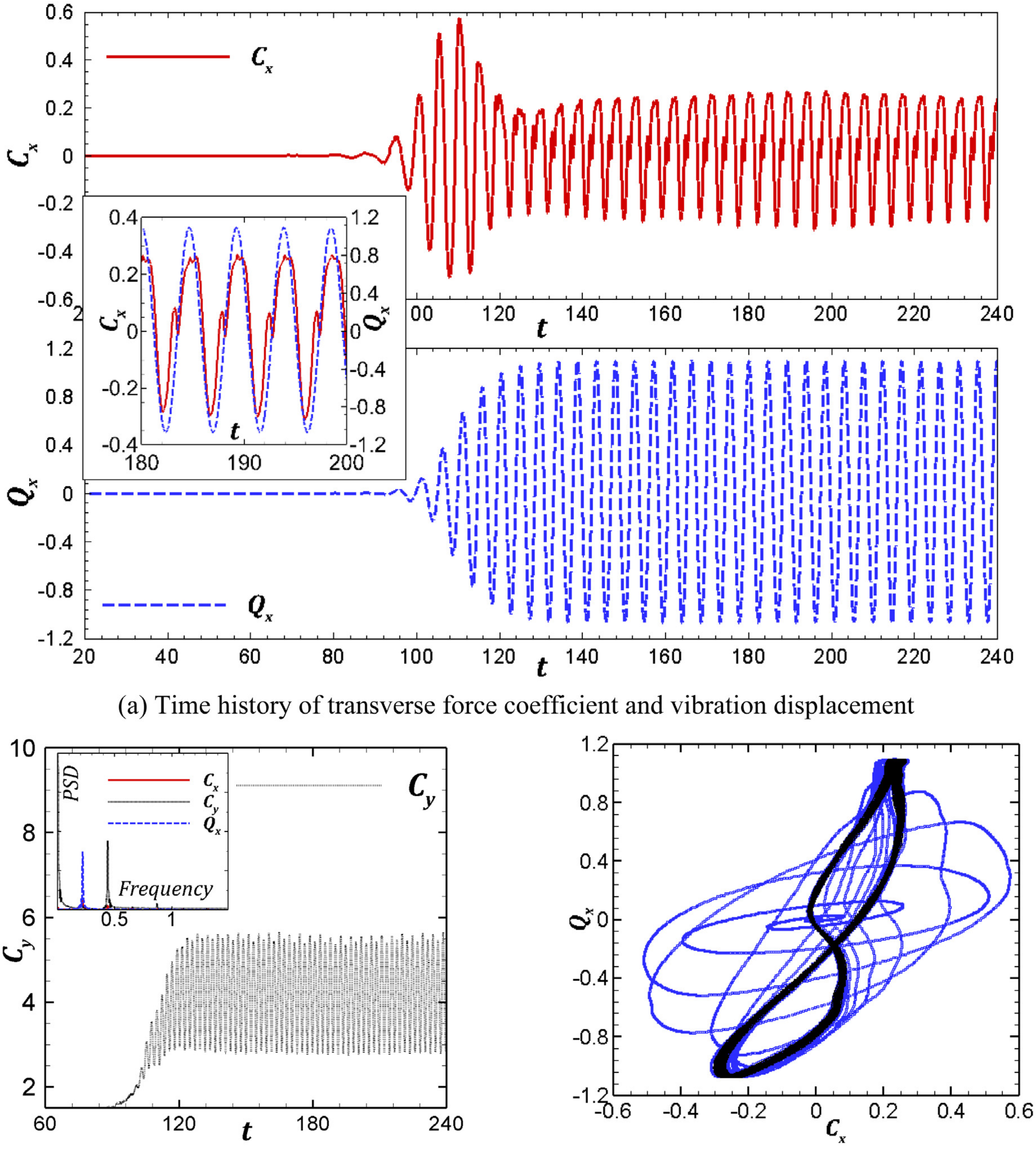

(a) Time history of transverse force coefficient and vibration displacement

(b) Drag coeffiicent and PSD

(c) Phase plot

Fig. 18. Cylinder of AR = 4 in unsynchronized regime, $U_{red} = 4.5$.

velocity deficit region extends from $y = 1.2$ to 2.5, in which v is positive but smaller than the incoming flow velocity. As y further goes to downstream, v is greater than the unity velocity and a velocity jet is formed afterwards. Note as *Ri* increases from 0 to Ri_c, the variation of the wake vortex structure went through four stages, W2S, 2S, Crossed-2S, and attached vortices.

4.3.3. Suppression of VIV of cylinders with various aspect ratios

The thermal effects on VIV suppression regarding to the vibration amplitude A_x and the time-averaged drag coefficient $\overline{C}_y$ as a function of *Ri* are presented in Fig. 29 for elliptic cylinders with the aspect ratio ranging from 0.7 to 4. The blue

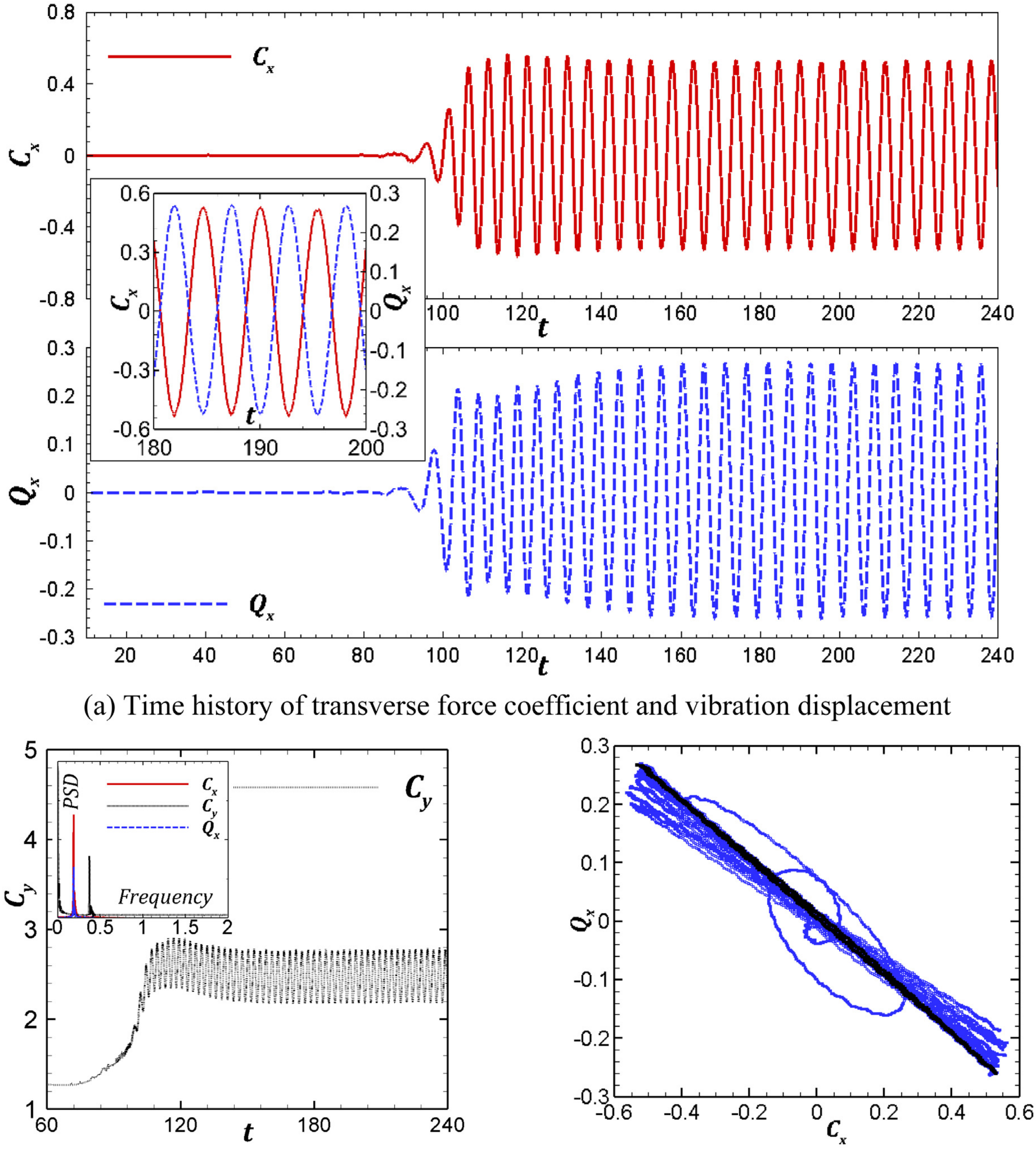

(a) Time history of transverse force coefficient and vibration displacement

(b) Drag coeffiicent and PSD

(c) Phase plot

Fig. 19. Cylinder of AR = 4 in unsynchronized regime, $U_{red} = 8$.

and red curves denote the lock-in region and the flexible region, respectively. The left plots show A_x as a function Ri, and the right plot is $\overline{C}_y$. Numerically, we set Ri_c as the Richardson number at which the vibration amplitude is 1% of the body major axis. The graphs can be used to visually justify where Ri_c is located.

Generally, as Ri increases from 0 to Ri_c, the VIV amplitude A_x decreases, as show in Fig. 29(a,c,e,g,i). Also, Ri_c rises with the increment of the aspect ratio, since A_x is also greater for cylinders with higher AR. For example, without thermal control ($Ri = 0$), A_x is 0.2 for an AR 0.7 cylinder in the lock-in regime, and A_x is 1.08 for an AR 4 cylinder in the lock-in regime. Once Ri_c is reached, the VIV is fully suppressed. The averaged drag coefficient $\overline{C}_y$ of the lock-in and flexible cylinders are

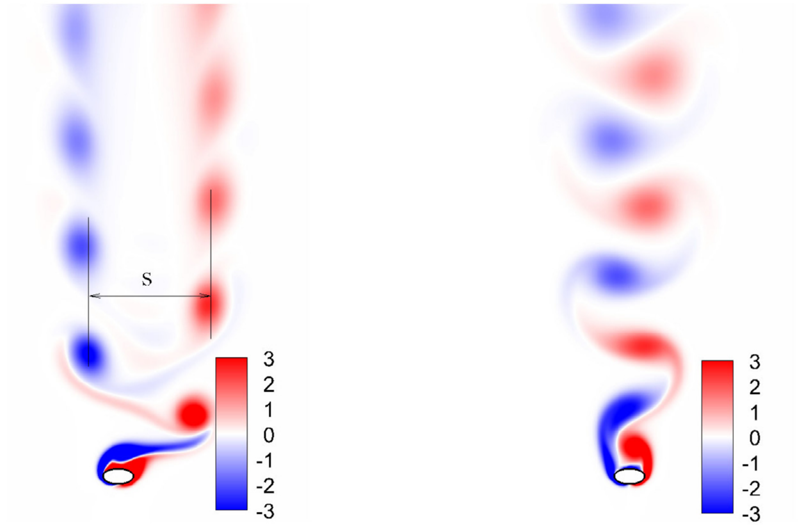

(a) $U_{red} = 4.5$ (b) $U_{red} = 8$

Fig. 20. Vorticity field of flow past AR 2 cylinder in (a) lock-in regime and (b) unsynchronized regime. The distance S between the two vortex columns is around 4*D* in lock-in regime.

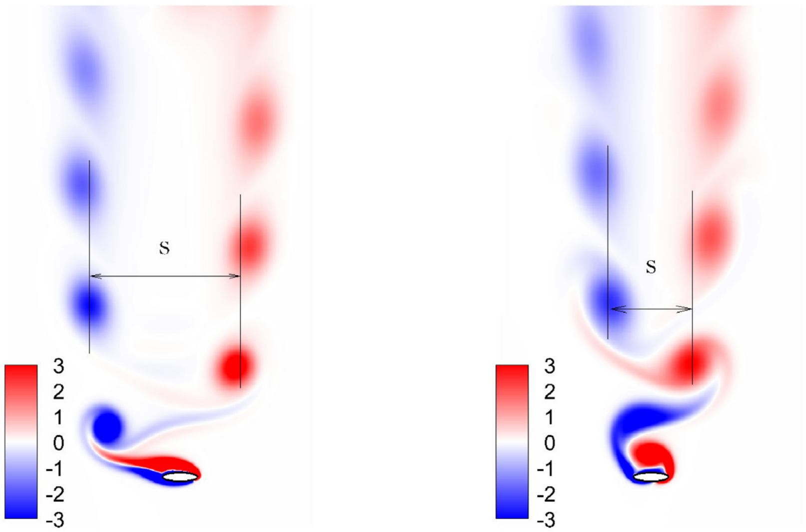

(a) $U_{red} = 4.5$ (b) $U_{red} = 8$

Fig. 21. Vorticity field of flow past AR 4 cylinder in (*a*) lock-in regime and (*b*) unsynchronized regime. The distance S between the two vortex columns is around 4.3*D* and 3*D* in lock-in and flexile regimes, respectively.

basically identical when Ri is above Ri_c (Fig. 29b,d,f,h,j), since the flow is independent of the reduced frequency U_{red} when VIV is fully suppressed.

For VIV in the lock-in region, the body experiences the minimum drag at Ri_c, indicating that Ri_c is the optimized Richardson number since both VIV suppression and the minimum drag are obtained. If Ri keeps increasing after Ri_c, $\overline{C}_y$ starts to rise for all ARs. For cylinders of AR ≥ 1, even though $\overline{C}_y$ increases after Ri_c, it can be seen (Fig. 29d,f,h,j) that $\overline{C}_y$ at high Ri is still smaller than $\overline{C}_y$ at zero Ri. For example, for a cylinder of with AR $= 4$ in lock-in regime (Fig. 29g), $\overline{C}_y$ at zero Ri is 4.21. It is reduced to 2.42 at Ri_c (Table 6), after which it increases with Ri and reaches to 3.17 at $Ri = 2$. This is 75.2% of $\overline{C}_y$ at zero Ri. However, for a cylinder with small AR such as 0.7, $\overline{C}_y$ can quickly surpass its zero Ri counterpart

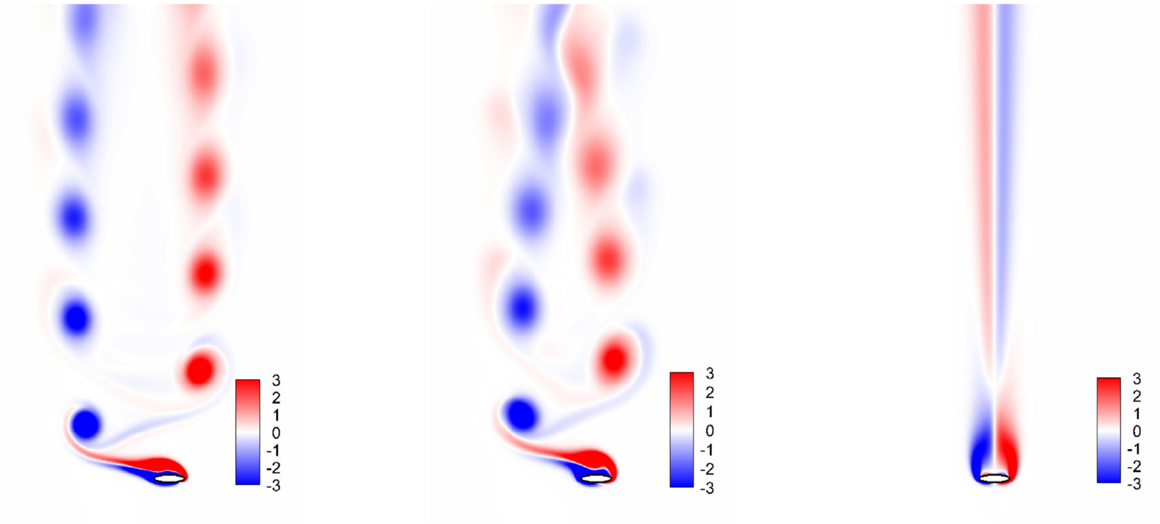

(a) $Ri = 0.4$ (b) $Ri = 0.8$ (c) $Ri = 0.93$

Fig. 22. Vortex structure of flow past an AR = 4 cylinder. Vortex shedding is suppressed when Richardson number reaches a critical value $Ri_c = 0.93$. $U_{red} = 4.5$, $M_{red} = 10$, $Re = 100$, $Pr = 7.1$, $t = 300$.

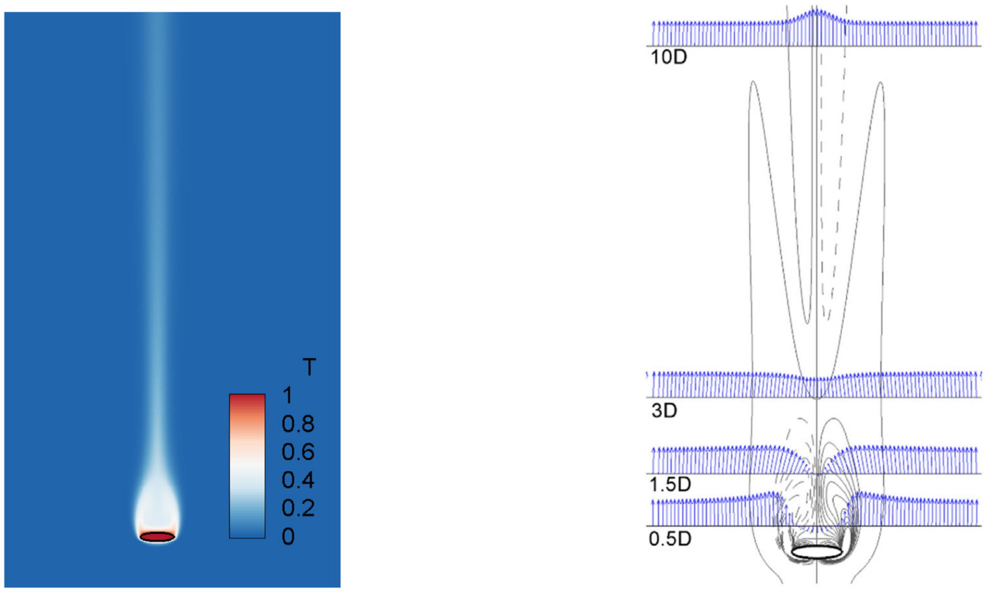

(a) (b)

Fig. 23. (a) Temperature field, and (b) velocity vector at certain sections of flow past an AR = 4 cylinder. $U_{red} = 4.5$, $M_{red} = 10$, $Re = 100$, $Pr = 7.1$, $t = 300$.

(Fig. 29b) if Ri keeps increasing beyond Ri_c. Therefore, for VIV in the lock-in regime, both A_x and $\overline{C}_y$ decrease until Ri_c is reached. Further increasing Ri causes unnecessary rising of $\overline{C}_y$.

For VIV in the unsynchronized regime, increasing Ri will suppress VIV, but it will also simultaneously increase $\overline{C}_y$, as shown in the red dash line in Fig. 29(b,d,f,h,j). The abrupt reduction of $\overline{C}_y$ at Ri_c in Fig. 29 (f,h,j) is due to the suppression of VIV. Beyond Ri_c, $\overline{C}_y$ is monotonically increases with Ri. When VIV is fully suppressed Ri_c, $\overline{C}_y$ is not the minimum for

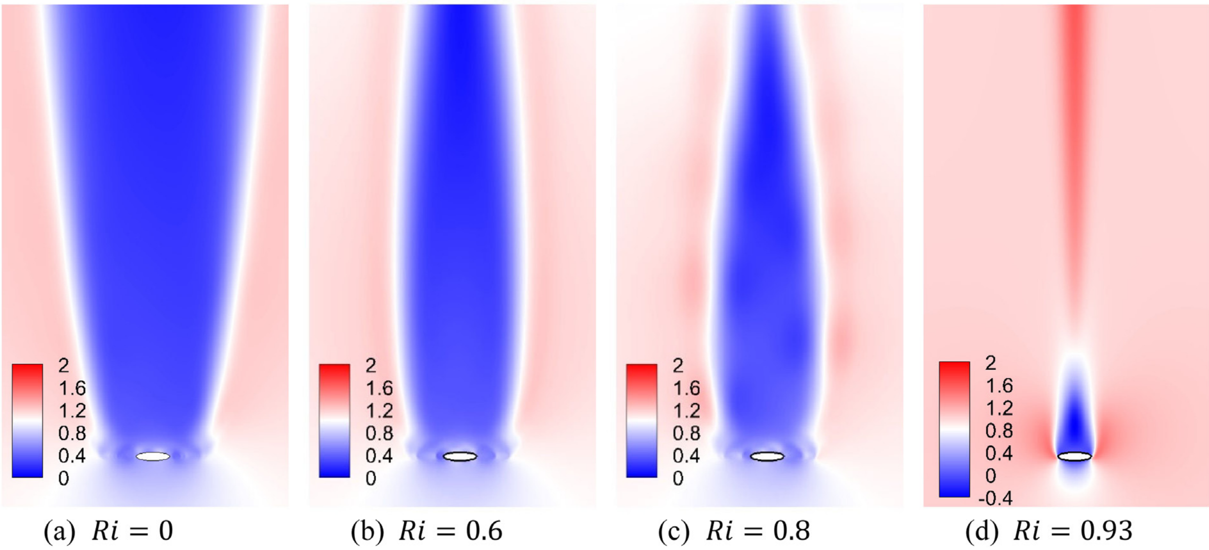

Fig. 24. Time-averaged velocity component v at various Ri for a cylinder with AR $= 4$ and $U_{red} = 4.5$.

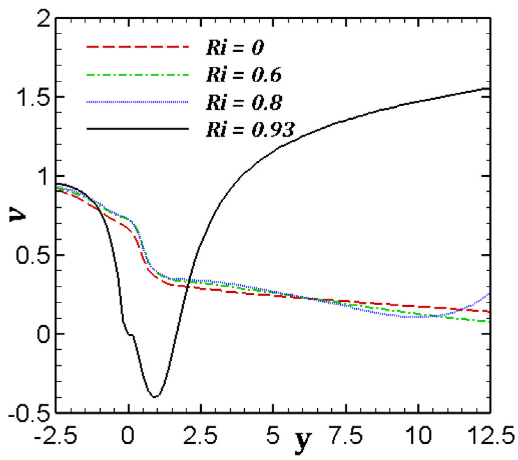

Fig. 25. Vertical velocity component v along the cylinder centerline, $U_{red} = 4.5$.

most of the cases (except the cylinder AR 2). Therefore, even though the thermal control can be used to fully suppress VIV in the unsynchronized regime, the drag coefficient may not be the minimum.

The critical Richardson number Ri_c of cylinders with various aspect ratios in lock-in and unsynchronized regimes are shown in Fig. 30. For cylinders with aspect ratio equal to or smaller than 2, Ri_c of unsynchronized regime is smaller than that of lock-in regime, i.e., it is easier to suppress VIV in the unsynchronized regime. For instance, Ri_c is 0.43 and 0.35 to suppress VIV of an AR2 cylinder, in lock-in and unsynchronized regimes, respectively.

For cylinders of aspect ratio 3 or 4, Ri_c of unsynchronized regime is higher than that of lock-in regime. For example, Ri_c is 0.93 and 1.5 for AR $= 4$ cylinders in the lock-in and the unsynchronized regime, respectively. For the AR 4 cylinder in lock-in regime, when Ri increases, the wake vortex structure remains as W2S, especially the near field, as shown in Fig. 21(a) and Fig. 22(a,b). The vortex shedding is abruptly suppressed near Ri_c. The wake experiences only two states: W2S and attached vortices. This abrupt change of flow properties in the wake can also be confirmed in Fig. 25, in which the variation of the time-averaged vertical velocity v is small as Ri increases from 0 to 0.8. The time-averaged vertical velocity v experiences an abrupt increase at Ri_c.

For the AR 4 cylinder in unsynchronized regime, increasing of Ri can only reduce the oscillation moderately. As Ri increases, the wake vortex structure gradually experiences four states: from W2S (Fig. 21b), 2S, Crossed-2S, to attached

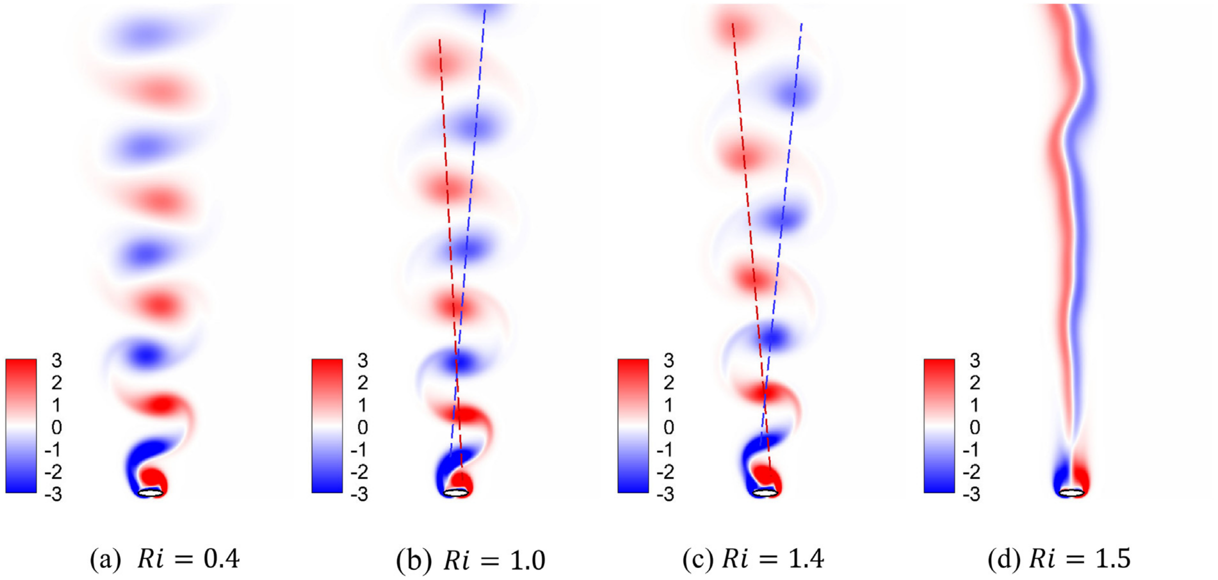

Fig. 26. Vortex structure of flow past an AR = 4 cylinder. Vortex shedding is suppressed when Richardson number reaches a critical value $Ri_c = 1.5$. $U_{red} = 8$, $M_{red} = 10$, $Re = 100$, $Pr = 7.1$, $t = 300$.

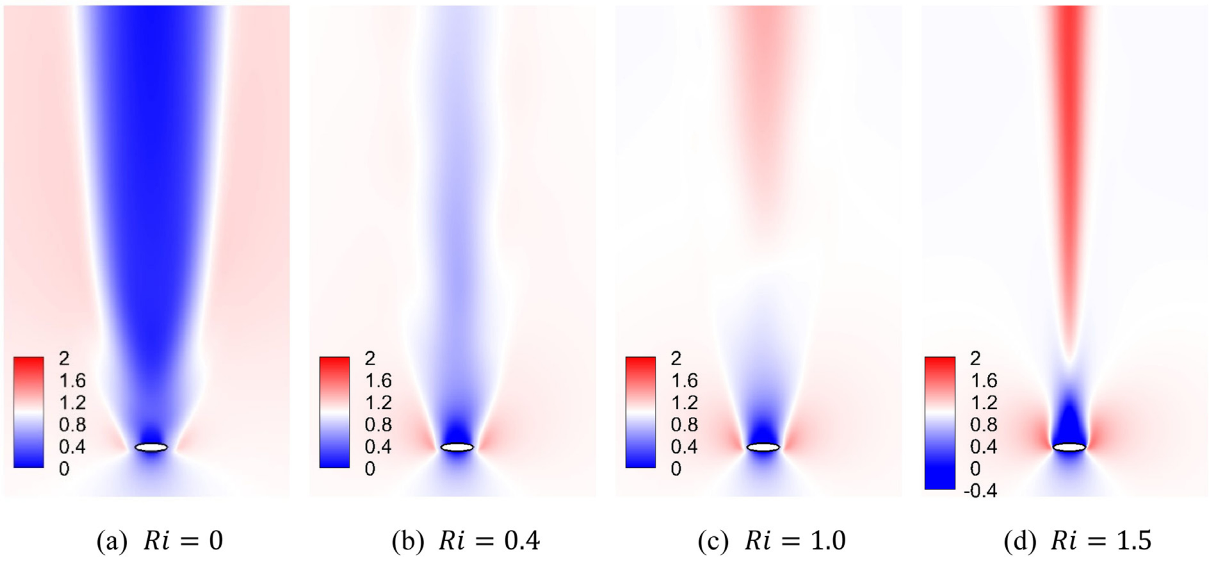

Fig. 27. Time-averaged velocity component v at various Ri for a cylinder with AR = 4 and $U_{red} = 8$.

vortices (Fig. 26). The corresponding time-averaged vertical velocity shown in Fig. 28 also confirms this gradual variation of flow properties in the wake. Thus, A_x slightly decreases of as Ri increases (Fig. 29i,). This property boosts Ri_c of the flexible AR 4 cylinder to as high as 1.5.

5. Conclusion

Vortex-induced transverse vibration of an elastically-mounted, elliptic cylinder at Reynolds number 100 was numerically studied. The aspect ratio ranging from 0.7 to 4 was considered. The reduced velocity was varied between 1 and 9. The high end of the reduced velocity corresponds to small stiffness structures in unsynchronized regime. The middle

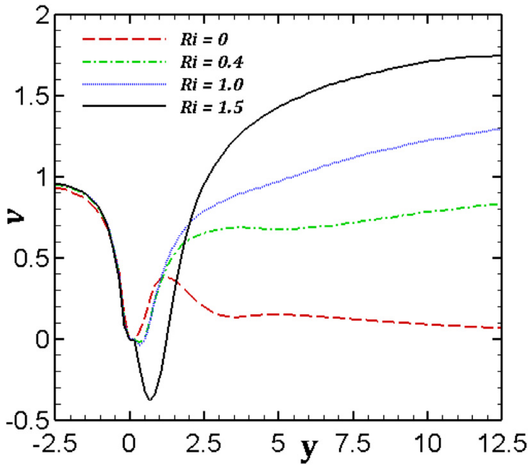

Fig. 28. Vertical velocity v along the cylinder centerline, $U_{red} = 8$.

reduced velocity corresponds to the lock-in regime. VIV in unsynchronized regime has small vibration amplitude; and the transverse force and the displacement oscillate out of phase. On the contrary, VIV in the lock-in regime has high vibration amplitude, and the transverse force and the displacement oscillate in phase in most of cases. As the aspect ratio of the elliptic cylinder increases, the VIV amplitude and the associated drag coefficient are also increased, for both the lock-in and the unsynchronized regimes.

To suppress VIV, the cylinder was heated to a uniform temperature. Thermal effects on VIV suppression were studied at various Richardson number *Ri*. As *Ri* increases, the vibration amplitude reduces. At the critical value Ri_c, the periodic vortex shedding and the induced vibration can be fully suppressed. The efficacy of VIV suppression using thermal control on circular cylinders with various reduced mass and Reynolds numbers has been demonstrated in our previous study (Wan and Patnaik, 2016). The current work mainly focuses on cylinders with various aspect ratios.

For VIV in the lock-in regime, the drag coefficient decreases and reaches the minimum at the critical Richardson number Ri_c. If *Ri* is further increased, the drag coefficient rises. Thus, Ri_c is an optimized Richardson number to achieve both VIV suppression and the minimum drag coefficient. The highest drag reduction of 50.2% can be obtained at Ri_c for the cylinder with aspect ratio 2. For VIV in the unsynchronized regime, even though the thermal control can suppress VIV, the drag coefficient, however, can be higher than that in the case of without control. Therefore, the thermal control is more appropriate to suppress VIV in the lock-in regime. When using thermal control to suppress the vibration of an AR 4 cylinder in the flexible VIV regime, we observed the cross-2S vortex structure, in which the near field typical 2S vortices crossed the centerline and switched sides after a few vibration cycles.

CRediT authorship contribution statement

Hui Wan: Methodology, Software, Investigation, Writing - original draft, Writing - review & editing. **Jeffrey A. DesRoches:** Investigation, Validation, Writing - original draft, Writing - review & editing. **Anthony N. Palazotto:** Supervision, Project administration, Writing - original draft, Writing - review & editing. **Soumya S. Patnaik:** Supervision, Resources, Project administration, Writing - original draft, Writing - review & editing.

Declaration of competing interest

The authors declare that they have no known competing financial interests or personal relationships that could have appeared to influence the work reported in this paper.

Acknowledgments

J.A.D. gratefully acknowledge funding, education, and support from AFRL/RQQI, USA and the Air Force Institute of Technology, USA. H.W. thanks CRCW grant from UCCS, USA, and computational resource from XSEDE program DMS180004.

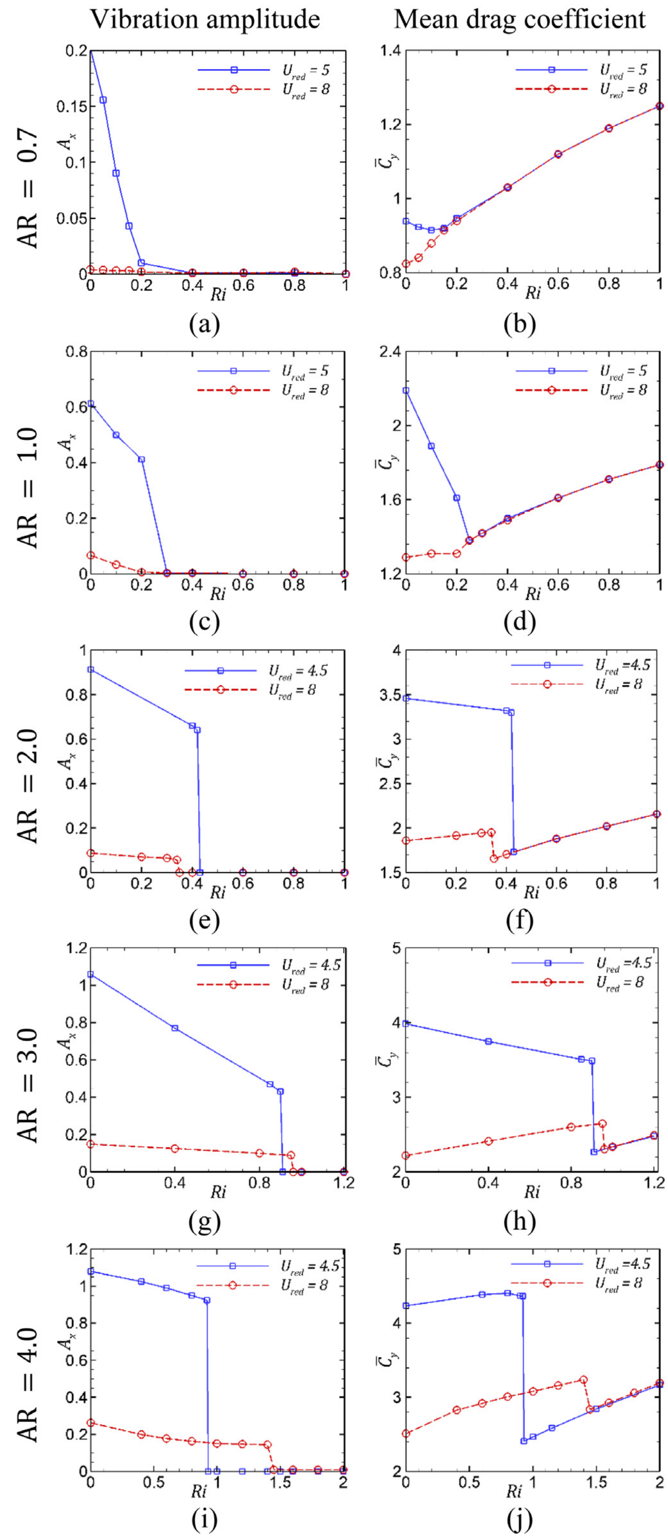

Fig. 29. Vibration amplitude (left) and mean drag coefficient (right) as *Ri* increases for cylinders with various ARs in lock-in and unsynchronized regimes.

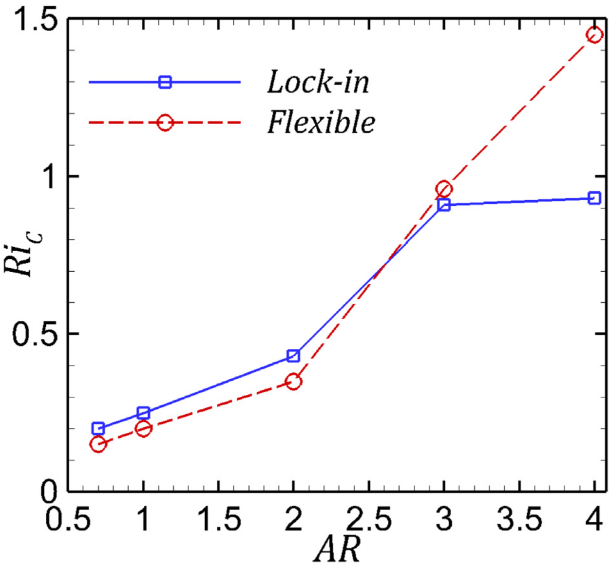

Fig. 30. Ri_c of cylinders with various aspect ratios in lock-in and unsynchronized regimes.

References

Adhikari, S., Rastogi, A., Bhattacharya, B., 2020. Piezoelectric vortex induced vibration energy harvesting in a random flow field. Smart Mater. Struct. 29, 035034.
Assi, G.R.S., Bearman, P.W., 2018. Vortex-induced vibration of a wavy elliptic cylinder. J. Fluids Struct. 80, 1–21.
Chang, K.-S., Sa, J.-Y., 1990. The effect of buoyancy on vortex shedding in the near wake of a circular cylinder. J. Fluid Mech. 220, 253–266.
Chen, W.L., Xin, D.B., Xu, F., Li, H., Ou, J.P., Hu, H., 2013. Suppression of vortex-induced vibration of a circular cylinder using suction-based flow control. J. Fluids Struct. 42, 25–39.
Dash, S.M., Triantafyllou, M.S., Alvarado, P.V.Y., 2020. A numerical study on the enhanced drag reduction and wake regime control of a square cylinder using dual splitter plates. Comput. & Fluids 199, 104421.
Franzini, G.R., Bunzel, L.O., 2018. A numerical investigation on piezoelectric energy harvesting from vortex-induced vibrations with one and two degrees of freedom. J. Fluids Struct. 77, 196–212.
Gabbai, R.D., Benaroya, H., 2005. An overview of modeling and experiments of vortex-induced vibration of circular cylinders. J. Sound Vib. 282, 575–616.
Garg, H., Soti, A.K., Bhardwaj, R., 2019a. Vortex-induced vibration and galloping of a circular cylinder in presence of cross-flow thermal buoyancy. Phys. Fluids 31, 113603.
Garg, H., Soti, A.K., Bhardwaj, R., 2019b. Vortex-induced vibration of a cooled circular cylinder. Phys. Fluids 31, 083608.
Griffith, M.D., Lo Jacono, D., Sheridan, J., Leontini, J.S., 2016. Passive heaving of elliptical cylinders with active pitching – From cylinders towards flapping foils. J. Fluids Struct. 67, 124–141.
Hover, F.S., Tvedt, H., Triantafyllou, M.S., 2001. Vortex-induced vibrations of a cylinder with tripping wires. J. Fluid Mech. 448, 175–195.
Kumar, D., Mittal, M., Sen, S., 2018. Modification of response and suppression of vortex-shedding in vortex-induced vibrations of an elliptic cylinder. Int. J. Heat Fluid Flow 71, 406–419.
Kwon, K., Choi, H., 1996. Control of laminar vortex shedding behind a circular cylinder using splitter plates. Phys. Fluids 8, 479–486.
Lee, Y.J., Qi, Y., Zhou, G., Lua, K.B., 2019. Vortex-induced vibration wind energy harvesting by piezoelectric MEMS device in formation. Sci. Rep. 9 (20404).
Leontini, J.S., Griffith, M.D., Lo Jacono, D., Sheridan, J., 2018. The flow-induced vibration of an elliptical cross-section at varying angles of attack. J. Fluids Struct. 78, 356–373.
Mittal, R., Iaccarino, G., 2005. Immersed boundary methods. Annu. Rev. Fluid Mech. 37, 239–261.
Navrose, Yogeswaran, V., Sen, S., Mittal, S., 2014. Free vibrations of an elliptic cylinder at low Reynolds numbers. J. Fluids Struct. 51, 55–67.
Newman, D.J., Karniadakis, G.E., 1997. A direct numerical simulation study of flow past a freely vibrating cable. J. Fluid Mech. 344, 95–136.
Sarpkaya, T., 2004. A critical review of the intrinsic nature of vortex-induced vibrations. J. Fluids Struct. 19, 389–447.
Serson, D., Meneghini, J.R., Carmo, B.S., Volpe, E.V., Gioria, R.S., 2014. Wake transition in the flow around a circular cylinder with a splitter plate. J. Fluid Mech. 755, 582–602.
Strykowski, P.J., Sreenivasan, K.R., 1990. On the formation and suppression of vortex 'shedding' at low Reynolds numbers. J. Fluid Mech. 218, 71–107.
Wan, H., Dong, H.B., Huang, G.P., 2012b. Hovering hinge-connected flapping plate with passive deflection. AIAA J. 50, 2020–2027.
Wan, H., Dong, H., Liang, Z., 2012a. Vortex formation of freely falling plates. 50th AIAA Aerospace Sciences Meeting Including the New Horizons Forum and Aerospace Exposition. American Institute of Aeronautics and Astronautics, Nashville, Tennessee.
Wan, H., Patnaik, S.S., 2016. Suppression of vortex-induced vibration of a circular cylinder using thermal effects. Phys. Fluids 28.
Wang, C., Tang, H., Duan, F., Yu, S.C.M., 2016a. Control of wakes and vortex-induced vibrations of a single circular cylinder using synthetic jets. J. Fluids Struct. 60, 160–179.
Wang, C., Tang, H., Yu, S.C.M., Duan, F., 2016b. Active control of vortex-induced vibrations of a circular cylinder using windward-suction-leeward-blowing actuation. Phys. Fluids 28, 053601.
Wang, H., Zhai, Q., Chen, K., 2019. Vortex-induced vibrations of an elliptic cylinder with both transverse and rotational degrees of freedom. J. Fluids Struct. 84, 36–55.
Williamson, C.H.K., Govardhan, R., 2004. Vortex-induced vibrations. Annu. Rev. Fluid Mech. 36, 413–455.

Zhao, J., Hourigan, K., Thompson, M.C., 2019. Dynamic response of elliptical cylinders undergoing transverse flow-induced vibration. J. Fluids Struct. 89, 123–131.
Zhu, H., Zhao, Y., Zhou, T., 2018. Numerical investigation of the vortex-induced vibration of an elliptic cylinder free-to-rotate about its center. J. Fluids Struct. 83, 133–155.